J. Fluid Mech. (2022), *vol*. 945, A7, doi:10.1017/jfm.2022.539

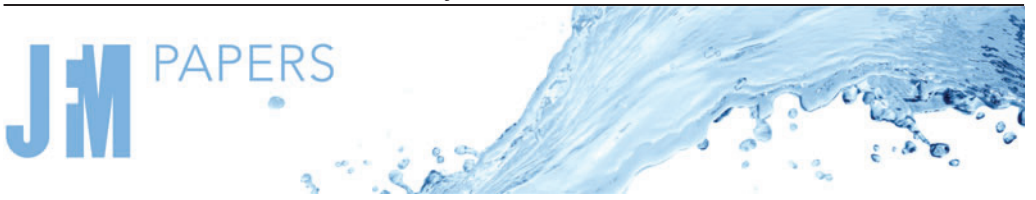

Characterization of bifurcated dual vortex streets in the wake of an oscillating foil

Suyash Verma[1] **and Arman Hemmati**[1],†

[1]Department of Mechanical Engineering, University of Alberta, Edmonton, AB T6G 2R3, Canada

(Received 7 October 2021; revised 23 May 2022; accepted 19 June 2022)

Wake evolution of an oscillating foil with combined heaving and pitching motion is evaluated numerically for a range of phase offsets (ϕ), chord-based Strouhal numbers (St_c) and Reynolds numbers (Re). The increase in ϕ from 90° to 180° at a given St_c and Re coincides with a transition of pitch- to heave-dominated kinematics that further reveals novel transitions in wake topology characterized by bifurcated vortex streets. At $Re = 1000$, each of the dual streets constitutes a dipole-like paired configuration of counter-rotating coherent structures that resemble qualitatively the formation of $2P$ mode. A new mathematical relation between the relative circulation of coherent dipole-like paired structures and kinematic parameters is proposed, including heave-based (St_h), pitch-based (St_θ) and combined motion (St_A) Strouhal numbers, as well as ϕ. This model can predict accurately the wake transition towards $2P$ mode characterized by a bifurcation, at low $Re = 1000$. At $Re = 4000$, however, the relationship was inaccurate in predicting the wake transition. A shear splitting process is observed at $Re = 4000$, which leads to the formation of reverse Bénard–von Kármán mode in conjunction with $2P$ mode. Increasing ϕ further depicts a consistent prolongation of the splitting process, which coincides with a unique transition in terms of absence and reappearance of bifurcated dipole-like pairs at $\phi = 120°$ and 180°, respectively. Changes in the spatial arrangement of $2P$ pairs observed consistently for oscillating foils with the combined motion constitute a novel wake transition that becomes more dominant at higher Reynolds numbers.

Key words: vortex shedding, wakes, swimming/flying

1. Introduction

Propulsive mechanisms for fish swimming have been studied extensively since the late 20th century (Lighthill 1969; Webb 1975; Videler 1993; Fish & Lauder 2005). The theoretical analysis and comprehensive review presented in these studies have provided us with fundamental understanding of undulatory motion for slender bodies (Lighthill 1969),

† Email address for correspondence: arman.hemmati@ualberta.ca

active and passive flow control in biological marine swimmers (Webb 1975; Colgate & Lynch 2004), and exploitation of flow in different environments (Fish & Lauder 2005). More recently, researchers have expanded their studies on locomotion of fish to examine the underlying mechanisms that have also been observed for flight of birds and insects (Bode-Oke & Dong 2020; Li, Dong & Zhao 2020). These provide insights into the fundamental phenomenon for the generation of dynamic force (i.e. lift, thrust and drag) under different biological conditions and kinematics. The conceptual advancements from these studies have been the prime motivator behind the ongoing innovations in marine propulsion, aerial flight technologies and novel energy harvesting systems (Wu *et al.* 2020).

Studies conducted specifically within the realm of hydrodynamic propulsion have also focused on how the motion of a fluid around a bluff body, such as a circular cylinder or hydrofoil, was utilized to harvest energy contained in the fluid and thereby generated a forward propelling force (Williamson & Roshko 1988; Koochesfahani 1989; Triantafyllou, Triantafyllou & Grosenbaugh 1993; Triantafyllou, Triantafyllou & Yue 2000). These active flow manipulations are attained mostly through the influence of oscillatory kinematics generally involved with a motion in one or more degrees of freedom (Koochesfahani 1989; Anderson *et al.* 1998; Godoy-Diana, Aider & Wesfreid 2008; Schnipper, Andersen & Bohr 2009; Cleaver, Wang & Gursul 2012; Lagopoulos, Weymouth & Ganapathisubramani 2019; Van Buren, Floryan & Smits 2019). Each kinematic regime is observed to coincide with specific spatio-temporal characteristics of wakes that can be associated with the nature of the force produced by the oscillating body (Anderson *et al.* 1998). Numerous studies exist that characterized extensively the oscillations with a single degree of freedom, such as pure heaving or pitching (Smits 2019). The coupled oscillation with two degrees of freedom had gained considerable attention recently on account of its greater complexity with additional motion parameters and their interdependence with induced changes in flows (Van Buren *et al.* 2019). Here, we aim to explore and characterize specific kinematic regimes for the coupled pitching and heaving motion of an oscillating hydrofoil, where the influence of phase offset (ϕ) between pitching and heaving motions on evolution of the wake is examined for a broad parameter space.

We review briefly some of the early prominent studies mentioned above. Williamson & Roshko (1988) described the formation of wake modes behind a transversely oscillating cylinder that had different spatial arrangement and temporal shedding of coherent structures. The peculiar modes observed with increasing transverse amplitude (A) and wavelength ratio (λ/d, where d is the diameter of the cylinder) constituted pairs of counter-rotating vortices shed in a one-half shedding cycle (Williamson & Roshko 1988). These modes were termed as $2P$, where two paired structures were shed in one oscillation cycle (Williamson & Roshko 1988). In a few other modes, such pairs also shed with additional isolated vortices, which were then categorized and termed as $2P + 2S$ or $P + S$, based on whether two or one isolated structures were shed in the wake (Williamson & Roshko 1988). Schnipper *et al.* (2009) also observed exotic wakes behind an oscillating foil that executed pure pitching motion. Within a range of trailing edge amplitude (A) and associated Strouhal number ($St_A = 2fA/U_\infty$, where f is the frequency of oscillation), their experiments depicted modes ranging through $2P$, $4P$, $4P + 2S$ and $8P$. The $2P$ mode observed within fixed parametric ranges for St_A and $A_D = 2A/D$ coincided with optimal values required for more efficient propulsion of fish (Muller, van den Boogaart & van Leeuwen 2008; Schnipper *et al.* 2009). Their study also evaluated the transition of $2P$ to $2S$ mode with increasing St_A. This transition was modelled mathematically in terms of the relative circulation strength of coherent structures formed at leading and trailing

edges of the foil (Schnipper *et al.* 2009). It suggested that an increase in St_A contributed to strengthening of the trailing edge vortex compared to the leading edge vortex. This phenomenon eventually led to an early merger between the shed structures, and thus a transition from $2P$ to $2S$ mode (Schnipper *et al.* 2009).

Similar to foils undergoing pure pitching, studies focusing on kinematics of purely heaving foils suggested the formation of deflected wake modes with increasing oscillation frequency, which included Modes A and B (Cleaver *et al.* 2011, 2012; Calderon *et al.* 2014). These modes were characterized primarily by dipole configuration of counter-rotating vortex structures with much closer proximity compared to those observed in paired vortices of $2P$ mode in wakes of pitching foils (Cleaver *et al.* 2011; Calderon *et al.* 2014; He & Gursul 2016). Cleaver *et al.* (2011) described dual branch configurations of wakes, Mode-1 and Mode-2, comprised of a dipolar formation of counter-rotating vortex structures. Cleaver *et al.* (2012) also characterized dipoles or couples that were comprised of counter-rotating structures with an equal circulation strength.

In addition to classifications of wakes highlighted above, an assessment for the association of spatial configurations of wakes and performance variation within specific kinematic regimes formed an integral part of some numerical and experimental studies. Das, Shukla & Govardhan (2016) investigated the variation in propulsive performance and characterization of wakes at increasing Reynolds numbers ($10 \leq Re \leq 2000$) and Strouhal numbers ($0 \leq St \leq 1$), using two-dimensional simulations of purely pitching foil. Their study revealed a steep increase in propulsive efficiency observed for increasing St. It was found to be associated with shift in the streamwise location at which the wake deflected behind the foil. Their wake map also revealed that the transition of wake from Bénard–von Kármán (BvK) to reverse Bénard–von Kármán ($rBvK$) preceded the drag-to-thrust transition for all Reynolds numbers. The experimental results of Van Buren *et al.* (2019) depicted an increased propulsive efficiency with changes in kinematics of the foil. They evaluated novel scaling relations of thrust and power of an oscillating foil, undergoing a combined heaving and pitching motion at $Re = 8000$. The propulsive benefits observed were aligned with earlier observations of Anderson *et al.* (1998), which related gains in performance with constructive interference between trailing and leading edge vortices at optimum phase lag or offset 90°. This study also offered deeper insights about the influence of the changing phase angle between pitching and heaving motion on the propulsive performance, which had not been investigated in detail previously. In particular, Van Buren *et al.* (2019) suggested that changes in ϕ influenced the motion in terms of either pitch- or heave-dominated kinematics, and therefore effected the propulsive performance. However, more extensive analysis is still needed to identify important features of wakes that show novel spatio-temporal characteristics due to changes in phase angle and resulting transitions in kinematics of oscillating foils.

Besides extensive experimental investigations (Van Buren *et al.* 2019), recent two-dimensional numerical studies by Lagopoulos *et al.* (2019) and Zheng *et al.* (2019) discussed the wake and performance metrics for a foil performing coupled two degrees of freedom oscillations, for a fixed phase angle 90° (or 270° in the reference frame of Van Buren *et al.* 2019). Verma & Hemmati (2021*b*) also described evolution of the primary wake structures of an oscillating foil in coupled heaving and pitching motion. However, this investigation was limited to $\phi = 270°$ and 330°, which corresponded to kinematic regimes for high propulsive efficiencies and production of greater thrust, respectively (Van Buren *et al.* 2019). Furthermore, these phase angles characterized primarily a pitch-dominated oscillatory motion, where the trailing edge amplitude was higher compared to the leading edge. Most recently, Cimarelli, Franciolini &

Crivellini (2021) conducted two-dimensional numerical simulations of pure heaving foil in order to investigate the role of kinematic and flow parameters in prompting smooth and sharp transition in configurations of wake. In the range of Reynolds numbers between 50 and 5000, they determined that increasing Re beyond the critical value 200 led to a transition in configuration of wake from $rBvK$ to a stable deflected mode. The wake then attained the $rBvK$ mode again (Cimarelli *et al.* 2021). These studies either had focused on oscillations with a single degree of freedom, or were limited to pitch-dominated mixed motions. As such, a very limited characterization of the wakes for heave-dominated coupled motion exists in the literature for flapping foils.

There also exist serious gaps in our knowledge related to wakes of oscillating foils undergoing combined pitching and heaving motion. To address these, our major goal in this study is to understand the novel wake characteristics when the phase offset between the heave and pitch motion increases from 0° to 180° for a given chord-based Strouhal number (St_c) and Reynolds number. This range of phase offset also presents a vivid transition of kinematics of foils from a pitch- to heave-dominated coupled oscillatory motion. In particular, we provide detailed evidence and insights into transition of wake topology towards bifurcated vortex streets characterized by dipole-like paired vortical structures. Quantitative and qualitative characteristics of evolution are described further for such streets that constitute dipole-like vortical pairs. A mathematical model for relative circulation strength of counter-rotating structures is then proposed in terms of Strouhal number based on trailing and leading edge amplitudes. This model characterizes particularly the behaviour of wake during coupled heaving and pitching kinematics. Finally, mean flow features associated with the bifurcated dual vortex streets are also highlighted in order to provide detailed insights on time-averaged spatial development of wake under such circumstances. The paper is arranged such that the problem and methodology are explained in § 2, followed by the discussion of results in § 3. Major conclusions are then presented in § 4.

2. Methodology

The flow around a teardrop foil (figure 1) with maximum thickness (D) to chord length (c) ratio $D/c = 0.1$ is examined numerically at a range of chord-based Strouhal numbers ($St_c = fc/U_\infty = 0.16$–$0.48$), amplitude-based Strouhal numbers ($0.06 \leq St_A \leq 0.34$) and Reynolds numbers ($Re = U_\infty c/\nu = 1000$–$4000$). Here, U_∞ is the freestream velocity, ν is the fluid viscosity, and f is the frequency of oscillations. Recent experimental studies of Van Buren *et al.* (2018, 2019) and Floryan *et al.* (2017), which focused on propulsive performance and scaling relations of underwater propulsors, suggested that the teardrop foil geometry represented a simplified model for fish tail fins. We further limited the detailed analyses of the wake characteristics to the cases $Re = 1000$ and 4000, where the wake features and transition effects were more profound without the additional complexities associated with higher Reynolds number flows (Zurman-Nasution, Ganapathisubramani & Weymouth 2020). This choice of Re also followed closely with assessments conducted by Godoy-Diana *et al.* (2008), Schnipper *et al.* (2009), Deng, Sun & Shao (2015), Das *et al.* (2016), Lagopoulos *et al.* (2019) and Cimarelli *et al.* (2021).

The foil oscillates with a combined heaving and pitching motion at a point located approximately $0.05c$ from the leading edge. Figure 1(a) depicts the oscillating foil, where heave and pitch amplitudes are denoted by h_L and θ_o, respectively. The resultant trailing edge amplitude is depicted as A_T. For this study, h_L/c and θ_o are fixed at 0.25 and 10°, respectively. Figure 1(b) further depicts the heave ($\dot{h}_L$) and effective (U_{eff}) velocities as

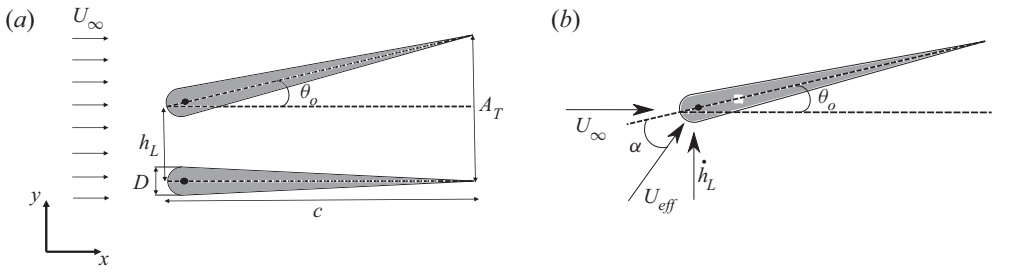

Figure 1. Schematics of the foil kinematics and resultant velocity at the leading edge during the motion.

seen by the leading edge of the foil. These would be helpful while modelling the vorticity production and circulation strength of vortex structures originating at the leading edge boundary layer. The phase offset (ϕ) varied from 0° to 270°, which resulted directly in a variation of trailing edge amplitude (A_T). The sinusoidal motion profiles of heave (h) and pitch (θ), where pitching has phase advancement ϕ relative to heaving, are represented using

$$h(t) = h_L \sin(2\pi ft), \tag{2.1}$$

$$\theta(t) = \theta_o \sin(2\pi ft + \phi). \tag{2.2}$$

On account of variation in ϕ and A_T, the Strouhal number ($St_A = 2fA_T/U_\infty$) also varied in the range specified in the previous paragraph, where the maximum and minimum St_A correspond to $\phi = 0°$ and 180°, respectively. Andersen *et al.* (2017) have indicated that interesting and significant transitions in the wake of flapping foils were observable within a Strouhal number range of $0.2 < St_A < 0.4$. This also coincides with the range corresponding to optimal propulsive efficiency in swimming mammals (Triantafyllou *et al.* 1993; Smits 2019). Further, the specified range of St_A had been observed to preserve the wake two-dimensionality of a flapping foil that involved a pure pitching or a pitch- or heave-dominated coupled motion setting (Zurman-Nasution *et al.* 2020). This further justified the parameter space considered in the current study.

Note that the most propulsively efficient phase offset of 90° according to Anderson *et al.* (1998), which was also employed by Zheng *et al.* (2019) and Lagopoulos *et al.* (2019), is equivalent to $\phi = 270°$ in the current study following the reference coordinate system employed by Van Buren *et al.* (2019).

2.1. *Numerical details*

The continuity and Navier–Stokes equations were solved directly using OpenFOAM, which is a finite-volume method that has been used extensively for simulating wake dynamics of oscillating foils and panels (Senturk & Smits 2018; Hemmati, Van Buren & Smits 2019; Zheng *et al.* 2019; Bose, Gupta & Sarkar 2021; Verma & Hemmati 2021*a*,*b*; Verma, Khalid & Hemmati 2022*b*). The oscillatory foil dynamics was modelled using the overset grid assembly (OGA) method, based on a stationary background grid and a moving overset grid that are merged for the simulation (Petra 2019). Extensive details of the method can be found in Verma & Hemmati (2020, 2021*b*).

The computational domain is depicted in figure 2, which highlights the C-type overset boundary containing the foil. The boundary conditions at the inlet were prescribed a uniform fixed velocity (Dirichlet) and a zero normal gradient (Neumann) for pressure. At the outlet, a zero-gradient outflow boundary condition was implied (Deng *et al.* 2015).

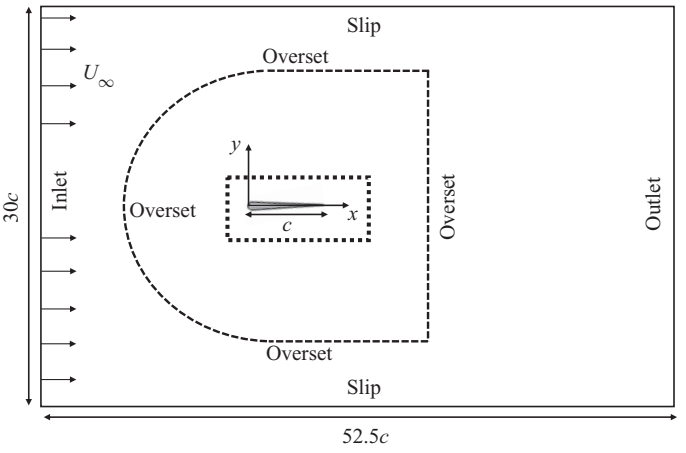

Figure 2. Schematics of the computational domain (not to scale) with boundary conditions.

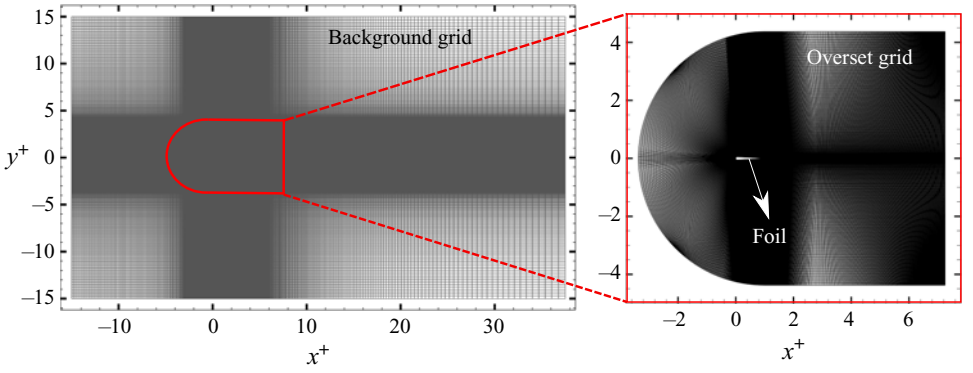

Figure 3. Schematics of the grid and overset grid assembly method.

The top and bottom walls are further prescribed a slip boundary condition that models effectively the open surface flows and resembled closely the experimental conditions (Hemmati *et al.* 2019; Van Buren *et al.* 2019). At the foil boundary, a no-slip condition for velocity and a zero-gradient condition for pressure was ensured. Figure 3 depicts further the non-homogeneous hexahedral grid comprising a C-type grid to model the foil geometry and motion. This region overlaps a rectangular background grid. Higher refinement was provided in critical overlapping regions, such that the near body vortex shedding and wake interactions were captured accurately. The grid expanded further towards the domain boundaries at an expansion factor of less than 1.02. The flow was solved using the overPimpleDyMFoam solver, which integrated the functionality of OGA and the PIMPLE algorithm. Second-order accurate backward and central difference schemes were employed for temporal and spatial discretizations, respectively (Senturk & Smits 2018). The momentum equations were solved using the preconditioned biconjugate gradient (PbiCGSTAB) method, whereas the preconditioned conjugate gradient (PCG) method was employed for the Poisson equation (Deng *et al.* 2015; Zheng *et al.* 2019).

A spatial convergence analysis was also completed at $Re = 8000$, $h_L/c = 0.25$, $\theta_o = 15^\circ$, $\phi = 270^\circ$ and $St_c = 0.67$. This enabled a comparative evaluation with experiments

Study	N_{total}	$\overline{C_T}$	$\Delta\overline{C_T}$	ϵ_T	$x =$	$1c$	$2.5c$	$5c$
Grid1	4.67×10^5	1.22	0.070	0.117	$\delta^* =$	4.29	4.41	6.18
Grid2	8.49×10^5	1.14	0.046	0.044	$\delta^* =$	2.53	3.39	6.36
Grid3	1.72×10^6	1.09	—	0.002	$\delta^* =$	1.58	2.03	3.16
Van Buren *et al.* (2019)	—	1.092	—	—	—	—	—	—

Table 1. Grid convergence analysis for the oscillating foil. Here, N_{total} represents the sum of hexahedral elements in the background and overset grids.

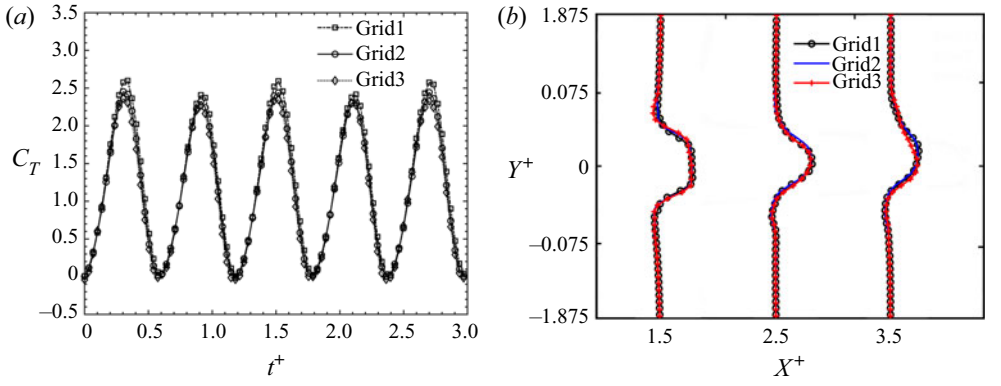

Figure 4. Comparison of (*a*) unsteady variation of C_T, and (*b*) cross-stream velocity profiles at increasing streamwise distance (x^+) for three grids.

of Van Buren *et al.* (2019). Table 1 and figure 4 summarize the grid convergence results involving three grids, where Grid1, Grid2 and Grid3 comprised approximately 4.7×10^5, 8.5×10^5 and 1.7×10^6 elements, respectively. Here, the ratio (δ^*) of minimum grid size element (Δx) to Kolmogorov scale (η) was kept below 10, within the critical region near the foil (see table 1). The Kolmogorov scale was calculated based on kinematic viscosity (ν) and the dissipation rate of turbulence kinetic energy (ϵ), given by the relation $\eta \approx (\nu^3/\epsilon)^{0.25}$ (Pope 2000). The first cell layer size also corresponds to $0.012c$, $0.007c$ and $0.004c$ for Grid1, Grid2 and Grid3, respectively. This is fairly similar to the study of Senturk & Smits (2018), and it is even finer (on order of magnitude) compared to the grid utilized by Zheng *et al.* (2019, 2020). The coefficient of thrust ($\overline{C_T} = \bar{T}/0.5\rho scU_\infty^2$), which was averaged over the final 10 oscillating cycles following the statistical convergence, was used as a quantitative estimate for spatial grid convergence. The relative error ($\epsilon_T = |\overline{C_{T,exp}} - \overline{C_T}|/\overline{C_{T,exp}}$) calculated with respect to the experimental results (Van Buren *et al.* 2019) was below 5 % for Grid2.

Figure 4 shows the instantaneous C_T variation and cross-stream distribution of mean streamwise velocity ($\overline{U_x^+}$) at increasing streamwise distance (X^+) for the three grids discussed in table 1. These results show clearly that the propulsive performance and wake characteristics of the foil are not sensitive to the spatial grid resolution. This further provided sufficient confidence to use Grid2 for our analysis. The time step size (δt) was also set, such that the ratio of eddy turnover time (τ_η) to δt for the smallest dissipative eddy (Pope 2000) yields at least 100 time steps. This ensured that our simulations had adequate resolution to capture essential turbulent characteristics, which aligned with

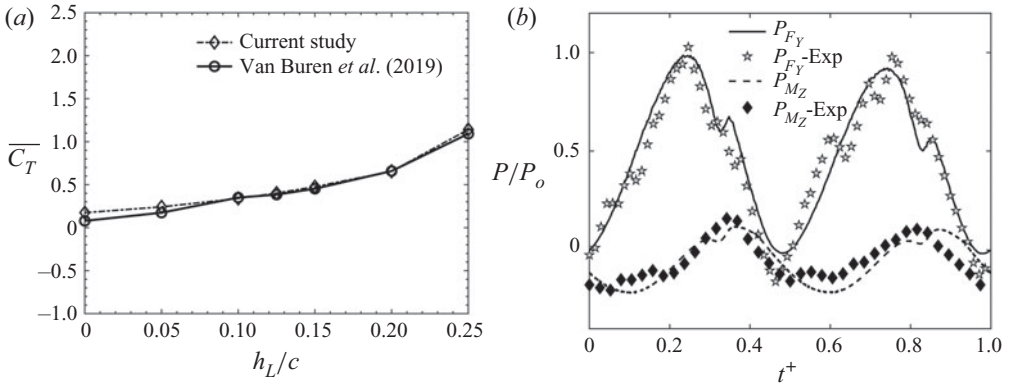

Figure 5. Comparison of (*a*) numerically obtained variation of $\overline{C_T}$, and (*b*) unsteady contributions of transverse force and pitch moment to the total input power of the oscillating foil with experiments of Van Buren *et al.* (2019).

the recommendations of Merrill & Peet (2017). The Courant number (Co) was also maintained below 0.5, similar to the simulations of Hemmati *et al.* (2019). Validation of the numerical solver with experiments (Van Buren *et al.* 2019) is also depicted in figure 5. Specifically, figure 5(*a*) shows that the computationally predicted $\overline{C_T}$, for $0 < h_L/c < 0.25$, $\theta_o = 15^\circ$, $\phi = 270^\circ$ and $St_c = 0.67$, was in good agreement with experiments of Van Buren *et al.* (2019). Figure 5(*b*) depicts further the instantaneous contribution of the transverse force (P_{F_Y}) and pitch moment (P_{M_Z}) to the total power (P_o) within one oscillation cycle. The computational predictions follow closely the quantified variation observed from experiments (Van Buren *et al.* 2019). The implications of two-dimensional simulations on the wake dynamics, compared to three-dimensional simulations, are also important within the scope of the current study. There are several studies (e.g. Das *et al.* 2016; Zheng *et al.* 2019; Zurman-Nasution *et al.* 2020) that revealed prominence of three-dimensional effects at $Re > 5000$ for oscillating foils. These studies also suggest that two-dimensional simulations are sufficient for capturing coherent flow structures at the relatively low Re considered here, e.g. 1000–4000. This range of Reynolds numbers aligns well with biological applications of swimming fish and small marine mammals (Godoy-Diana *et al.* 2008; Deng *et al.* 2015; Smits 2019). We have verified thoroughly that three-dimensional effects do not affect our analyses by completing a sensitivity study (besides our grid-sensitivity study and Kolmogorov scale ratio analyses) on three- versus two-dimensional simulations. However, the results are not shown here, for brevity, since they align clearly with the observations noted in the previous studies mentioned above.

Extensive efforts for verification and validation of the numerical solver with respect to domain size, spatial and temporal grid, OGA solver and boundary conditions can be found in Hemmati *et al.* (2019) and Verma & Hemmati (2020, 2021*b*).

3. Results and discussions

We begin by looking at the kinematics of the oscillating foil at increasing phase offset, chord-based Strouhal number and Reynolds number. In particular, these aspects are helpful in evaluating and modelling production of vorticity, and therefore the circulation strength for vortical structures. The shedding of these structures also coincides with the transition of a pitch- to heave-dominated coupled motion. We will then provide a qualitative discussion

on the transition and formation mechanisms of peculiar wake modes for increasing ϕ. This reveals the transition to bifurcated dual vortex street characterized by dipole-like paired vortices. Quantification of evolutionary characteristics, such as circulation strength and the separation distance between the shed vortical structures, is then evaluated in order to model the formation of wake mode, and transition in spatial topology with respect to the kinematics of oscillating foil. Initially, the wake analyses are focused on the case $Re = 1000$, which allows for a more detailed and vivid characterization of coherent structures. This is then expanded to a higher Reynolds number $Re = 4000$, wherein effects of Reynolds numbers are expected to be negligible (Das *et al.* 2016; Senturk & Smits 2019; Gungor & Hemmati 2021). Finally, the mean flow characteristics are evaluated, which highlight spatio-temporal features of wake that are common to the configuration of dual vortex street characterized by dipole-like pairs.

3.1. *Evaluation of kinematics*

The kinematics of oscillating foil in combined heaving and pitching motion is described within the range $0^\circ \leq \phi \leq 270^\circ$ at $0.16 \leq St_c \leq 0.48$. Instantaneous variations in trailing and leading edge amplitudes (a_T^+, h_L^+), and effective angle of attack (α), are depicted in figure 6 for one oscillation cycle, whereas the effect of increasing ϕ on a_T^+ and α is particularly observable in figures 6(*a*,*c*). Figure 6(*d*) depicts further variations in the peak angle of attack (α_o) with respect to increasing phase offset and St_c. The effective angle of attack for a foil with combined heaving and pitching motion is the resultant of both pitch- and heave-induced angle of attack (Lagopoulos *et al.* 2019). This is expressed mathematically as

$$\alpha = -\theta - \arctan\left(\dot{h}/U_\infty\right), \tag{3.1}$$

where $\dot{h}$ is the heave velocity of the foil. The variation of ϕ, corresponding to the peak angle of attack (i.e. $\phi = 90^\circ$), is consistent for increasing St_c.

The maximum a_T^+ as observed from figure 6(*a*) is attained for $\phi = 0^\circ$, which then decreases with ϕ approaching 180°. Increasing ϕ from 180° to 270° results in a higher peak a_T^+ within one oscillation cycle. On comparing the ratio of peak a_T^+ and h_L^+ with changing ϕ, it can be deduced that a smooth shift from pitch- to heave-dominated kinematics occurs with the phase offset approaching 180°. Then it reverts back to the pitch-dominated motion as ϕ increases beyond 180°. Our understanding about the influence of variations in such kinematics on evolution of wakes is still incomplete and therefore needs more attention. Moreover, the variation in α also depicts an increase in its peak, which then decreases to a minimum at $\phi = 270^\circ$. This is also observed in figure 6(*d*). The peak angle of attack holds considerable importance in terms of governing the dynamics of leading edge vortex and stall characteristics of the oscillating foil (Visbal 2009; Carr 2012). In order to investigate these aspects, specifically when a transition occurs from pitch- to heave-dominated coupled motion of a foil, we now discuss newly identified important observations with respect to evolution of wake that coincides with the aforementioned transition in kinematic regimes.

3.2. *Evaluation of wake mode transition at Re = 1000*

To understand the configuration of wake and its transition for a range of phase offset, amplitude and St_c at $Re = 1000$, we draw representative wake maps shown in figure 7.

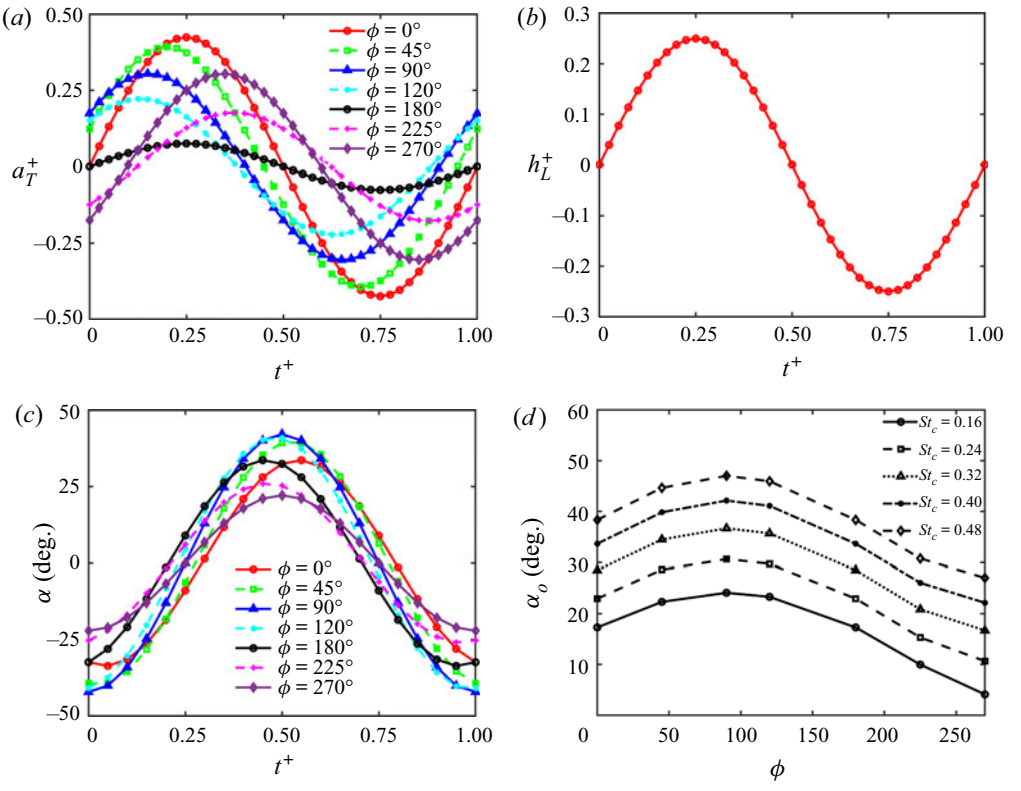

Figure 6. Temporal variation of (*a*) trailing edge amplitude (a_T^+), (*b*) leading edge (heave) amplitude (h_L^+), and (*c*) instantaneous α, within one single oscillation cycle. (*d*) Variation of peak α with respect to ϕ and St_c.

Specifically, figures 7(*a*) and 7(*b*) correspond to phase spaces characterized by ϕ versus St_c and A_c versus St_c, respectively. Figure 7(*b*), in particular, allows a comparison of transitions in wake topology with studies conducted on oscillating foils in pure pitching motion (Schnipper *et al.* 2009). The nomenclature of wake modes is also aligned with the studies conducted by Williamson & Roshko (1988) and Schnipper *et al.* (2009), which considered the number of shed vortical structures in one oscillation cycle for a cylinder and teardrop foil, respectively. For St_c below 0.32 in figure 7(*a*), it is observed that three wake modes corresponding to wavy Bénard–von Kármán (*wBvK*) (Lentink *et al.* 2008), $2P + 2S$ and $2P$, (Schnipper *et al.* 2009) are prominent at $Re = 1000$. More details of the wake categorization and transition at $Re = 1000$ can also be found in Verma & Hemmati (2022). For $St_c = 0.4$ and $Re = 1000$, the heave-dominated kinematics corresponding to $90° \leq \phi \leq 180°$ also depicts the dominance of $2P$ mode along with a characteristic bifurcation (marked by *B* in figure 7*a*) noticed between the two shed vortex pairs of $2P$, particularly at $\phi = 180°$. A transition from *rBvK* to *BvK*, followed by the similar bifurcation of $2P$ pairs, is further observed at $St_c = 0.48$.

It is worthwhile to observe if such wake mode transitions in terms of number of shed vortex structures, or characteristic bifurcations of shed $2P$ pairs, could coincide with a threshold value of St_A, as investigated by Schnipper *et al.* (2009), who focused particularly on purely pitching foils. Schnipper *et al.* (2009) observed that the transition from $2P$ to standard von Kármán ($2S$) mode coincided with the iso-line represented by $St_A = 0.11$. Furthermore, the transition of $2S$ to *rBvK* mode coincided with the line for $St_A = 0.18$

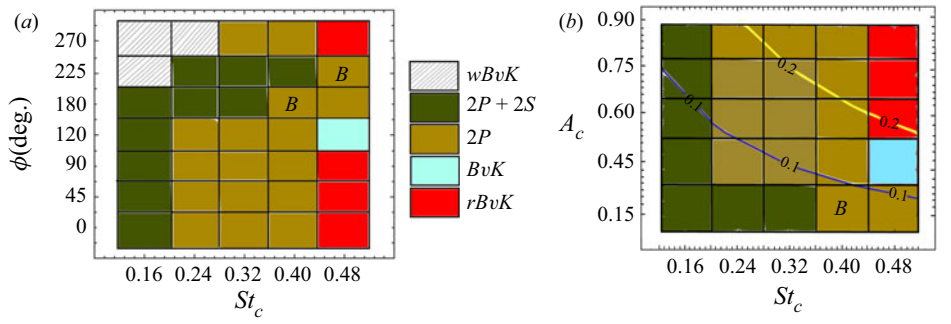

Figure 7. Phase map representation of identified wake modes at increasing St_c, ϕ and A_c for $Re = 1000$.

(Schnipper *et al.* 2009). In order to evaluate such coinciding transitions of wake modes with iso-lines of constant St_A in our study, we explain the wake modes at $Re = 1000$ on an A_c–St_c phase space diagram shown in figure 7(*b*). Here, A_c is the normalized trailing edge amplitude calculated as $2A_T/c$. The product of A_c and St_c yields lines of constant St_A on the phase space represented in figure 7(*b*). The two iso-lines drawn on the phase diagram correspond to $St_A = 0.1$ and 0.2, respectively. The range between the observed iso-lines coincides with $2P$ mode. The region beyond $St_A = 0.2$ marks a transition towards *rBvK* mode. Such findings therefore reveal a close resemblance to the observations reported by Schnipper *et al.* (2009). The transition from $2P$ mode to *rBvK* also goes through a *BvK* type or standard von Kármán wake mode as observed at $St_c = 0.48$. Further, the bifurcation of $2P$ pairs is found to lie below the line of $St_A = 0.1$, whereas increasing St_A beyond 0.1 does not reveal any bifurcations on the phase diagram. Besides the similarity observed in the trends of transition in wake mode configuration, with increasing St_A, the bifurcation of $2P$ pairs observed at some kinematic settings also reveals a qualitative similarity with the visualizations of $2P$ mode by Schnipper *et al.* (2009) and Andersen *et al.* (2017). However, specific details and features of the topological transitions in spatial arrangements of vortex structures, constituting the $2P$ mode, were not identified or investigated. We will therefore provide in-depth qualitative and quantitative descriptions of the characteristics of evolution while the $2P$ mode undergoes transitions in spatial topologies and encounters bifurcation of shed vortex pairs at certain kinematic settings observed in figure 7.

The wake formations at increasing ϕ are depicted in figure 8, at $Re = 1000$ and $St_c = 0.4$. A dominant shedding of counter-rotating vortex pairs in each half oscillation cycle is observed commonly for all the cases presented here. However, the changes in spatial configurations of paired structures are observed for increasing ϕ. At $\phi = 0^\circ$, a $2P$ mode (Williamson & Roshko 1988; Schnipper *et al.* 2009) appears, which is characterized by horizontally pointed pairs. The counter-rotating vortex structures TEV_{ac} and LEV_c, marked on figure 8(*a*), represent a $2P$ vortex pair. Here, subscripts *ac* and *c* denote the anticlockwise and clockwise rotating vortical structures, respectively. Another shed structure, LEV_{ac}, undergoes mutual interaction with the leg of TEV_{ac}. It is important to mention here that the abbreviations TEV_s and LEV_s denote the coherent structures formed at the trailing and leading edge of the foil, respectively. For the pitch-dominated motion profile at $\phi = 0^\circ$ (see figure 6), TEV_{ac} is stronger than LEV_{ac} based on their circulation strength and size in figure 8(*a*). It results eventually in the merger of similar sign LEV_s and TEV_s of the neighbouring pairs, traversing downstream in the wake. A similar $2P$ configuration was observed and discussed previously by Williamson &

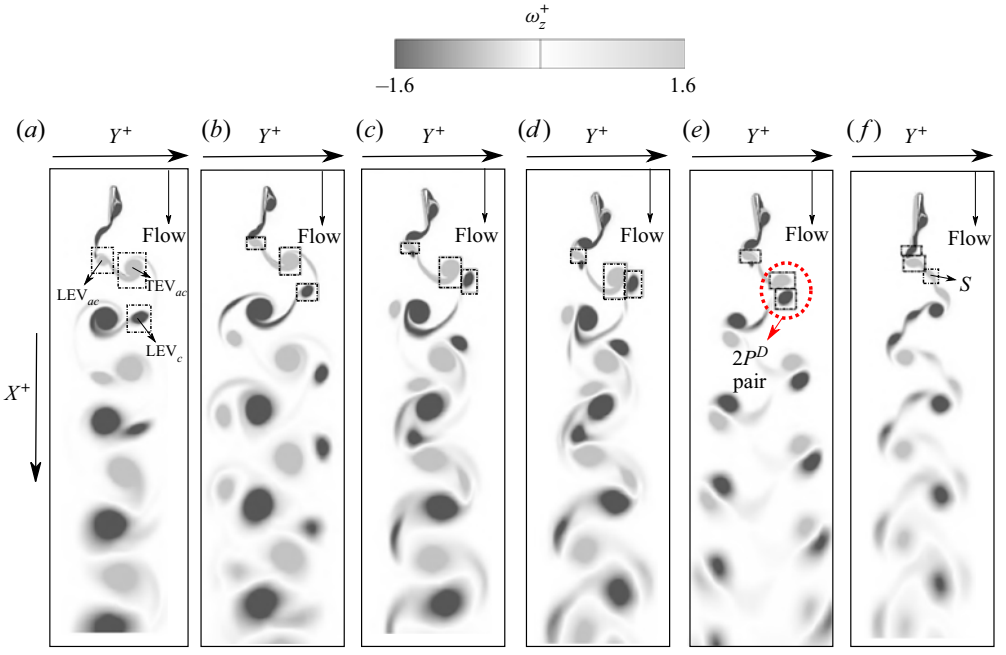

Figure 8. Wake modes at increasing ϕ and $Re = 1000$. Panels (a–f) represent ϕ corresponding to 0°, 45°, 90°, 120°, 180° and 225°, respectively, while $St_c = 0.4$.

Roshko (1988), Schnipper *et al.* (2009) and Hultmark, Leftwich & Smits (2007) in the wake of a transversely oscillating cylinder, a pitching foil and flexible robotic fins in sinusoidal oscillations, respectively. These $2P$ modes have also presented similarities in spatial configurations of thrust-producing wakes by swimming fish (Muller *et al.* 2008; Schnipper *et al.* 2009).

In order to elaborate further on the effects of increasing ϕ, we observe that at $\phi = 45°$, $2P$ vortex pairs are tilted and point in the upstream direction. No noticeable merger or interaction is observed between the neighbouring structures of these pairs, as shown in figure 8(b). These pairs also advect symmetrically along the wake centreline. The shed TEV possesses higher strength of circulation, in a qualitative sense, similar to the observations made at lower ϕ. Quantitative assessments for circulation are, however, presented in the next subsection for understanding the effects of changing ϕ on generation of vorticity. Moreover, wake formation at increasing ϕ up to 90° depicts shedding of counter-rotating vortices with a decreased separation distance (ζ) between their centres compared to the cases with lower values of ϕ. A similar observation can be made for $\phi = 120°$, where resemblance to dipole-like $2P$ pairs now become more vivid. We refer to such vortex pairs as $2P^D$ pairs in order to highlight them as dipole-like paired configurations, which appear in stark contrast to the $2P$ pairs observed at $\phi = 0°$ and 45°, respectively. Also, the wake still possesses a symmetry with respect to its centreline until $\phi = 120°$. Beside mutual interaction and merger of vortices, we do not observe any bifurcation of the shed pairs and dipole-like ($2P^D$) structures observed at increasing ϕ. However, two vortex streets constituting fully developed $2P^D$ pairs diverge away from the wake centreline with ϕ approaching 180° (see figure 8e). Structures forming such fully developed dipole-like configurations possess similar strengths of circulation and size, which was also reported

by Cleaver *et al.* (2012), Calderon *et al.* (2014), He & Gursul (2016) and Verma & Hemmati (2021*b*). Experimental studies of Cleaver *et al.* (2012) and Calderon *et al.* (2014) discussed the formation of dipoles and couples behind oscillating foils in purely heaving motion and further explained their prominent association and coincidence with deflected wake modes (i.e. Mode A or Mode B). Here, the dual vortex streets seen at $\phi = 180^\circ$ in figure 8(*e*) retain a symmetry along the wake centreline. This observation could indicate qualitatively that the entrainment effects of shed dipole-like structures (Calderon *et al.* 2014) are equally balanced, thus preventing the overall wake deflection in the upward or downward direction as noted in previous studies (Cleaver *et al.* 2012; Calderon *et al.* 2014). Increasing ϕ to 225°, as shown in figure 8(*f*), depicts an absence of diverging vortex streets, where trailing edge vortices are more stretched in the streamwise direction. An additional single vortex highlighted as S in figure 8(*f*) is also shed with a coincident shedding of a $2P$ pair. This mode therefore falls in the category of $2P + 2S$ (Williamson & Roshko 1988; Schnipper *et al.* 2009). It is now evident that while the bifurcation of $2P^D$ pairs resembles the observed $2P$ mode configuration of Schnipper *et al.* (2009), an elaborate evaluation is still warranted in order to understand the transitioning spatial topologies of $2P$ mode shown in figure 8. Furthermore, the kinematics investigated by Schnipper *et al.* (2009) followed a pure pitching motion rather than a combined heaving and pitching motion assumed in our current study.

3.3. *Formation mechanism of $2P^D$ pairs and symmetric bifurcation*

We now examine the formation process of $2P^D$ pairs at $Re = 1000$ by assessing the temporal evolution of shed vortical structures for the case $St_c = 0.4$ and $\phi = 180^\circ$. This parameter space is selected based on observations in figures 7(*a*) and 8(*e*), which allows for a better examination and characterization of bifurcations observed in $2P$ mode. The snapshots representing contours of spanwise vorticity (ω_z^+), at each quarter phase of an oscillation cycle, are illustrated in figure 9. At the beginning of an oscillation cycle (i.e. at $t = 0$) in figure 9(*a*), a developed $\mathrm{LEV1}_c$ is located close to the trailing edge, where $\mathrm{TEV1}'_{ac}$ is formed in the previous half oscillation cycle. At $t = T/4$ in figure 9(*b*), $\mathrm{LEV1}_c$ is detached from the trailing edge, where a new anticlockwise $\mathrm{TEV1}_{ac}$ starts forming behind the foil. Also, a new $\mathrm{LEV2}_{ac}$ appears developed at approximately the mid-chord region. $\mathrm{LEV1}_c$ forms a dipole-like paired configuration with $\mathrm{TEV1}_{ac}$ at the end of the half oscillation cycle (i.e. $t = T/2$) in figure 9(*c*), while $\mathrm{LEV2}_{ac}$ is on the brink of detachment from the trailing edge. With the oscillations proceeding to $t = 3T/4$ in figure 9(*d*), the first dipole-like pair ($D1$) is observed, which consists of vortical structures $\mathrm{LEV1}_c$ and $\mathrm{TEV1}_{ac}$. Simultaneously, a new trailing edge structure ($\mathrm{TEV2}_c$) begins to form and pairs with $\mathrm{LEV2}_{ac}$, which is now detached from the trailing edge. By the end of one oscillation cycle in figure 9(*e*), $\mathrm{TEV2}_c$ and $\mathrm{LEV2}_{ac}$ form a second dipole-like pair ($D2$). Both $D1$ and $D2$ are marked in figure 9(*e*). This description of the formation mechanism of $2P^D$ pairs is quite similar to that of a $2P$ pair observed in the wake of oscillating cylinders (Williamson & Roshko 1988) and foils (Schnipper *et al.* 2009; Andersen *et al.* 2017) with a single degree of freedom motion. Such $2P$ pairs were also seen in wakes corresponding to $\phi = 0^\circ$ in this study, as observed in figures 8(*a*) and 13(*a*). However, what distinguishes the $2P^D$ pair observed at $\phi = 180^\circ$ from the previously discussed $2P$ pairs is the approximate equality of circulation strength and size of the fully developed leading and trailing edge vortical structures ahead of their complete detachment from the foil's trailing edge. On account of these features, the mutual induced velocity of the dipole-like pair contributes to its movement away from the wake centreline, thus leading to the bifurcated dual vortex streets observed in figure 8(*e*). The dipole-like formation is also different from the dual

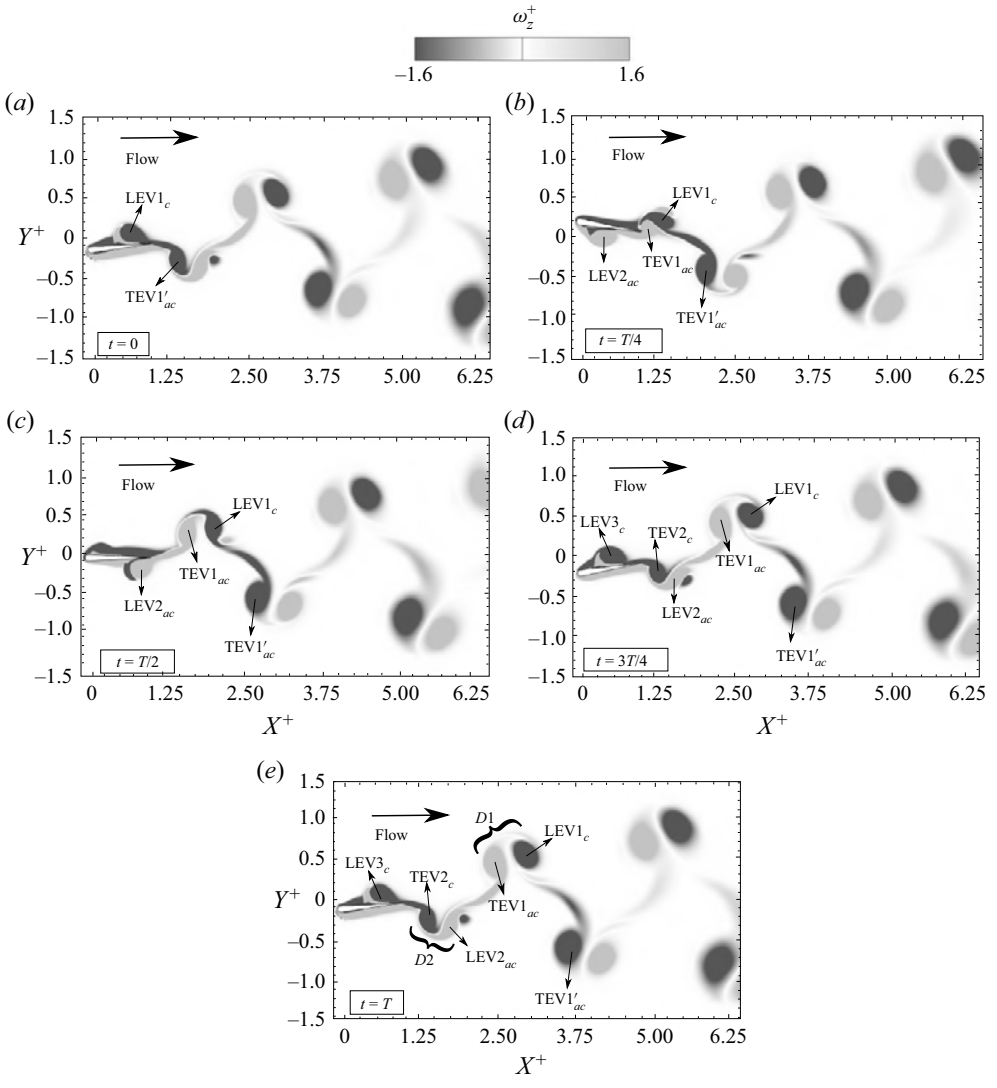

Figure 9. Temporal snapshots representing contours of $\omega_z^+ = \omega_z c/U_\infty$, and depicting formation of a $2P^D$ pair and bifurcation within the $2P$ mode at $St_c = 0.4$, $\phi = 180^\circ$ and $Re = 1000$.

branch Mode-1 described by Cleaver *et al.* (2011) for purely heaving foils. There, the dipole configuration constituted a weak trailing edge structure and another collective structure that was formed on account of a merger between strong leading and trailing edge vortices. This collective structure was formed and shed within one half oscillation cycle. In the case of $2P$ mode characterized by a fully developed $2P^D$ pair, we do not observe the formation of any collective structure similar to those reported by Cleaver *et al.* (2011). The above described process, therefore, hints at a spatial wake topology that is unique to foils with a combined heaving–pitching motion with different characteristics in terms of the vortex pair configuration, despite similarities in their formation process.

The above mentioned details of formation mechanism further allow us to relate the correspondence of the $2P^D$ pairs to the heave-dominated regime at $Re = 1000$

(see figure 7*a*). As observed here, only heave-dominated cases at $Re = 1000$ present a viable scenario, where the generated trailing and leading edge vorticities attain equal circulation strength and size after getting detached from the foil's trailing edge. It results in a net induced velocity of the dipole-like pair, pushing it away from the wake centreline and thus leading to bifurcations. As the kinematics transition to the pitch-dominated regime, the trailing edge vorticity gains enough strength relative to the leading edge vorticity that an eventual merger between similar sign structures occurs (see figure 8*a*). Hence it leads to a symmetric *rBvK* wake profile. Quantitative assessment described in the next subsection provides further evidence for our qualitative observations described above.

3.4. *Quantitative assessment of evolution characteristics*

The quantitative assessment of circulation strength ($\Gamma^+ = \Gamma/U_\infty c$) and separation distance between the centres of vortices ($\zeta^+ = \zeta/c$) can provide deeper insights into changes in evolution characteristics of the shed vortex structures with increasing ϕ at $Re = 1000$. These would also help us to understand particular features associated with changes in spatial topology of $2P$ wake, and appearance of bifurcations of $2P^D$ pairs. Specifically, we focus on the computed values of Γ^+ and ζ^+ just at the instance (shown in figure 8) when the counter-rotating vortex structures form pairs ahead of the foil's trailing edge. The estimation process for Γ involves calculating the surface integral of vorticity on a rectangular contour window using

$$\Gamma = \iint_S (\nabla \times V) \cdot d\boldsymbol{S}. \tag{3.2}$$

To calculate ζ, the location of maximum vorticity magnitude, within the rectangular window surrounding the vortex, is evaluated for each structure that form either a co-rotating or counter-rotating pair. The coordinates of centres (X, Y) are then used to find ζ:

$$\zeta = \sqrt{(X_2 - X_1)^2 + (Y_2 - Y_1)^2}, \tag{3.3}$$

where subscripts 1 and 2 indicate the centre coordinates of two similar-sign or counter-rotating vortical structures, respectively. Figure 8 depicts three windows around vortex structures TEV_{ac}, LEV_c and LEV_{ac}. TEV_{ac} and LEV_c form a pair of counter-rotating vortices, which eventually transitions to a dipole-like configuration as ϕ increases to 180°. TEV_{ac} and LEV_{ac} also undergo mutual interaction on account of their similar sense of rotation. These aspects further motivate us to understand the evolution of marked vortex structures, quantitatively.

Figure 10 shows the variation of circulation (Γ^+) and separation distance (ζ^+) with increasing ϕ for the heave-dominated kinematic settings ($\phi = 45°$–$180°$), since the major focus is on characterizing the bifurcated vortex street observed for $2P$ mode in this range of ϕ. As seen from figure 10(*a*), Γ^+ for TEV_{ac} drops consistently as ϕ increases from 45° to 180°. However, the paired vortex structure LEV_c depicts an opposite trend compared to TEV_{ac}, although the variation of Γ^+ is not as significant as in case the of TEV_{ac}. Despite the observed variations for these paired vortex structures, the newly shed LEV_{ac} depicts no changes with respect to increasing ϕ. This signifies clearly that the dominant evolution characteristics of a leading edge vortex remain approximately similar as it attains a paired configuration with the TEV, while kinematics transition from a pitch-based motion setting to a heave-dominated oscillation. The trailing edge vorticity,

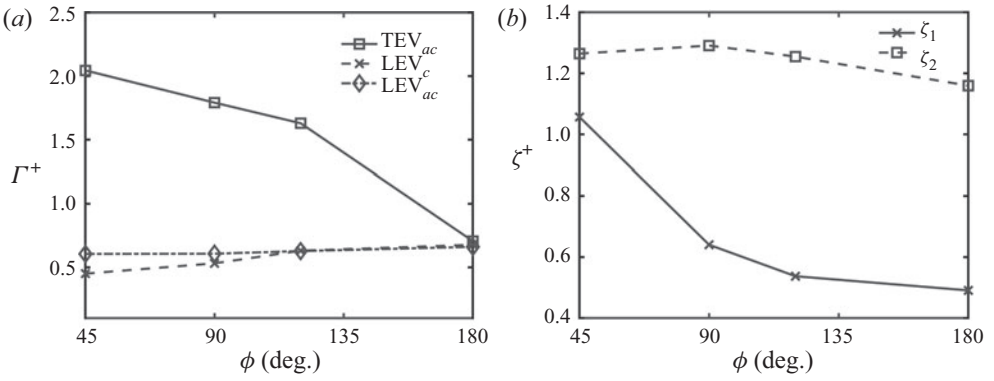

Figure 10. Variation of (*a*) circulation strength (Γ^+) and (*b*) separation distance (ζ^+) between counter-rotating and co-rotating vortex structures (highlighted in figure 8), with respect to ϕ.

however, is influenced greatly by the changes in trailing edge amplitude that were discussed previously for figure 6(*a*). The variation of ζ_1 and ζ_2, corresponding to the distance calculated between counter-rotating (LEV_c and TEV$_{ac}$) and co-rotating (LEV_{ac} and TEV_{ac}) vortex structures, is depicted further in figure 10(*b*). Similar to the qualitative discussion provided with respect to figure 8, we observe a decrease in ζ_1 as ϕ increases from 45° to 180°. On the other hand, ζ_2 shows an increase up to $\phi = 90°$, followed by a slightly decreasing trend towards $\phi = 180°$. The birfurcated vortex streets observed at $\phi = 180°$, which were characterized qualitatively by a fully developed dipole-like configuration, do possess a reduced separation distance between the counter-rotating vortex structures, along with their equal magnitude of Γ^+. Comparing these quantitative characteristics to the dipoles observed in deflected wakes of purely heaving and pitching foils (Cleaver *et al.* 2012; Calderon *et al.* 2014; Deng *et al.* 2015; He & Gursul 2016), the dipole-like $2P^D$ pairs constituting bifurcated wake streets also resemble similar evolution characteristics. However, the resultant wake still possessed a symmetry along the wake centreline, which therefore differs from the deflected wake modes observed previously (Cleaver *et al.* 2012; Calderon *et al.* 2014; Deng *et al.* 2015).

To understand further the transition from a paired configuration of counter-rotating structures with unequal circulation to the dipole-like arrangement characterized by equal strength structures ($2P^D$ pairs), we model mathematically the circulation estimates of a single leading edge vortex and trailing edge vortex at the instant of their shedding from the foil's trailing edge. This will also highlight any existing dependence of vortex evolution characteristics on ϕ. A single leading edge vortex structure is formed as a result of boundary layer roll-up near the leading edge, on one side of the foil. Hence its circulation estimation (Γ_{LEV}) can be obtained by calculating the vorticity transport in the boundary layer (Schnipper *et al.* 2009). This transport also assumes no-slip conditions on the foil, while considering contributions from the freestream (U_∞) and heave velocity ($\dot{h}$) at the leading edge (see figure 1). Similar assumptions were also in place for the models developed by Schnipper *et al.* (2009), although their analysis was limited to pitching motion and did not include the dependence on heave velocity. Based on the estimation of vorticity production in the boundary layer, given by Tietjens, Prandtl & Rosenhead (1957), we can calculate Γ^+ for a leading edge vortex just at the instant of its shedding in one half oscillation cycle using the relation

$$\Gamma_{LEV} = \tfrac{1}{2}\int_0^{T/2} (U_\infty^2 + \dot{h}^2)\,\mathrm{d}t. \tag{3.4}$$

Here, U_∞ represents the freestream velocity, while the heave velocity ($\dot{h}$) could be evaluated using the time derivative of (2.1). The integral can be subdivided as

$$\Gamma_{LEV} = \frac{1}{2}\left[\frac{U_\infty^2 T}{2} + \int_0^{T/2} h_o^2 4\pi^2 f^2 \cos^2(2\pi f t)\,\mathrm{d}t\right], \tag{3.5}$$

$$\Gamma_{LEV} = \frac{1}{2}\left[\frac{U_\infty^2 T}{2} + h_o^2 4\pi^2 f^2 \frac{1}{8}\left(\frac{\sin(2\pi f T)}{\pi f} + 2T\right)\right]. \tag{3.6}$$

The sin term evaluates to zero in the above equation, which therefore simplifies the expression to

$$\Gamma_{LEV} = \frac{U_\infty^2}{4f} + \frac{h_o^2 \pi^2 f}{2}. \tag{3.7}$$

Here, f represents the frequency of oscillation (i.e. $f = 1/T$). Further, using the foil diameter (D) and diameter-based Strouhal number ($St_D = fD/U_\infty$), we can again rewrite the last expression as

$$\Gamma_{LEV} = \frac{D^2 U_\infty + 2\,St_D^2\,U_\infty h_o^2 \pi^2}{4D\,St_D}. \tag{3.8}$$

Now, the circulation for the trailing edge vortex (Γ_{TEV}) can be estimated in a way similar to that followed by Schnipper *et al.* (2009), where they assumed that the freestream contribution to the vorticity is negligible. The expression can be written as

$$\Gamma_{TEV} = \tfrac{1}{2}\left(\int_0^{T/2} U_{TE}^2(t)\,\mathrm{d}t\right) \approx \tfrac{1}{2}\pi^2 A_T^2 f. \tag{3.9}$$

In terms of St_D and $A_D = 2A_T/D$, we can further rewrite the above expression as

$$\Gamma_{TEV} \approx \tfrac{1}{2}\pi^2 A_D^2\,St_D\,DU_\infty. \tag{3.10}$$

Now, in order to obtain an approximate estimate for the ratio of Γ for the leading and trailing edge vortex structures, we can divide (3.10) by (3.8). This ratio can be represented in its final form:

$$\frac{\Gamma_{TEV}}{\Gamma_{LEV}} \approx \left[\frac{2\pi^2 A_D^2}{\dfrac{1}{St_D^2} + \dfrac{2h_o^2\pi^2}{D^2}}\right]. \tag{3.11}$$

Here, the second term in the denominator is a constant value since the heave amplitude is not varying in our study. We can denote it as $\kappa = 2h_o^2\pi^2/D^2$. Also, after making some more simplifications to the above expression, we can also obtain a dependence on the amplitude-based Strouhal number ($St_A = 2fA_T/U_\infty$), thus

$$\frac{\Gamma_{TEV}}{\Gamma_{LEV}} \approx \frac{1}{2}\left[\frac{\pi^2\,St_A^2}{1 + \kappa\,St_D^2}\right]. \tag{3.12}$$

The above expression clearly highlights that at a constant St_D, dependence of the ratio $\Gamma_{TEV}/\Gamma_{LEV}$ on St_A is quite similar to the case of a pitching foil developed by

(Schnipper *et al.* 2009), although with a difference in constant of proportionality. We can still modify the above relationship to further obtain a dependence on the heave-based Strouhal number, $St_h = 2fh_o/U_\infty$. This formulation can be applied for cases where the variation of heave amplitude is also taken into account. This relationship becomes

$$\frac{\Gamma_{TEV}}{\Gamma_{LEV}} \approx \left[\frac{\pi^2\, St_A^2}{2 + \pi^2\, St_h^2}\right]. \tag{3.13}$$

By relating (3.13) to the qualitative depiction of wake modes on the A_c–St_c phase diagram in figure 7(*b*), we identify that there is a wake mode transition from $2P$ to *rBvK* type with increasing St_A from 0.1 to 0.2 and beyond. This is consistent with the observations of Schnipper *et al.* (2009), who found that a similar rise in relative strength of trailing edge structures was responsible for transition of wake from $2P$ to an *rBvK* mode. We can also relate this derived model to our quantitative details of kinematics (figure 6) and circulation estimates depicted in figure 10(*a*), at constant $St_h = 0.2$ and $St_c = 0.4$. Specifically, the kinematics indicated that with increasing ϕ from 45° to 180°, the peak trailing edge amplitude decreases to a minimum. This would result in a decrease in St_A, which, based on (3.12) and (3.13), should lead to a decrease in Γ_{TEV}. Ahead of $\phi = 45°$, the variation of Γ_{TEV} in figure 10 confirms this qualitative trend based on the strength of fully developed TEV_{ac}. Note that the parameters St_D and St_h are kept as constants in (3.12) and (3.13), respectively. The bifurcation of dipole-like vortex pairs ($2P^D$ pairs) within $2P$ mode can be also be linked to (3.13). As stated, when St_A reduces on account of increasing ϕ, the relative trailing edge circulation strength (Γ_{TEV}) also decreases. At the specific St_A (corresponding to $\phi = 180°$ and $St_c = 0.4$ in our phase space diagram), $\Gamma_{TEV}/\Gamma_{LEV}$ at the instance of shedding is such that the fully developed $2P^D$ pairs, ahead of their complete detachment from foil's trailing edge, constitute vortex structures of equal Γ^+ and lowest ζ. This was confirmed quantitatively in figure 10(*a*) wherein we see an equal magnitude of $\Gamma^+_{TEV_{ac}}$ and $\Gamma^+_{LEV_c}$ at $\phi = 180°$, $St_c = 0.4$ and $St_h = 0.2$. This contributes towards a transverse induced velocity leading to advection of the $2P^D$ pairs away from the wake centreline, thus causing bifurcation.

It is clear that the approximations for circulation ratio obtained in Schnipper *et al.* (2009) for purely pitching motion and (3.13) are quite comparable when St_h is constant. However, (3.13) still provides a valid and easy extension of the previous approximation (Schnipper *et al.* 2009) for an oscillating foil in coupled heaving and pitching motion, as considered here. Thus far, the validity of the proposed model is qualitatively interpreted only in terms of its accuracy in predicting the trend between relative circulation strength ($\Gamma_{TEV}/\Gamma_{LEV}$) and St_A for cases corresponding to heave-dominated kinematics at $Re = 1000$ and $St_h = 0.2$ (figure 7). In order to evaluate quantitatively the model's predictive capability at a wider parameter space, an approximate relationship is derived for the relative circulation strength in terms of ϕ, by transforming St_A into heave-based (St_h) and pitch-based (St_θ) Strouhal numbers. This is achieved by evaluating the vector addition of St_h and St_θ (Van Buren *et al.* 2019), and incorporating the phase offset ϕ between the pitch and heave motion. This is represented as

$$St_A^2 = St_h^2 + St_\theta^2 + 2\, St_h\, St_\theta \cos\phi. \tag{3.14}$$

Here, St_θ is defined as $2fc\theta_o/U_\infty$. Substituting (3.14) in (3.13), we obtain

$$\frac{\Gamma_{TEV}}{\Gamma_{LEV}} \approx \left[\frac{\pi^2\left(St_h^2 + St_\theta^2 + 2\, St_h\, St_\theta \cos\phi\right)}{2 + \pi^2\, St_h^2}\right]. \tag{3.15}$$

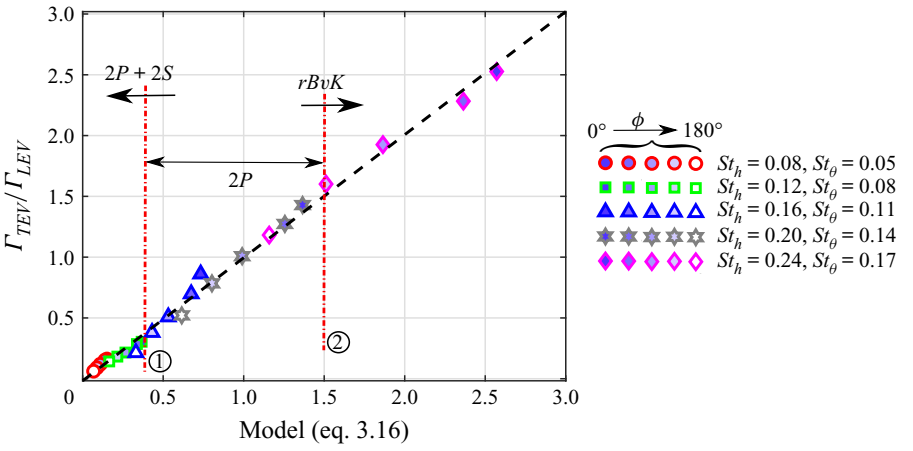

Figure 11. Scaling of estimated $\Gamma_{TEV}/\Gamma_{LEV}$ and model (3.16) outputs at increasing St_h, St_θ and ϕ.

Now we introduce coefficients (c_n) in each term of (3.15), to account for the multiplicative constants similar to the approach followed by Van Buren *et al.* (2019) and Verma, Freeman & Hemmati (2022*a*). The resulting expression is therefore written as

$$\frac{\Gamma_{TEV}}{\Gamma_{LEV}} = \left[\frac{c_1\, St_h^2 + c_2\, St_\theta^2 + c_3\, St_h\, St_\theta \cos\phi}{c_4 + c_5\, St_h^2}\right]. \tag{3.16}$$

The coefficients c_n are determined by performing linear regression over the entire parameter space represented in the phase maps (see figure 7). The ranges of St_h, St_θ and ϕ correspond to $0.08 \leq St_h \leq 0.24$, $0.05 \leq St_\theta \leq 0.17$ and $0^\circ \leq \phi \leq 180^\circ$. Figure 11 depicts plots for calculated estimates of $\Gamma_{TEV}/\Gamma_{LEV}$, determined through numerical simulations, and output of the expression represented by right-hand side of (3.16). The coefficients correspond to $c_1 = 2.02$, $c_2 = -0.51$, $c_3 = 0.97$, $c_4 = 0.11$ and $c_5 = -0.96$. As is evident in figure 11, we observe a collapse of $\Gamma_{TEV}/\Gamma_{LEV}$ and the model outputs (3.16), which therefore indicates a reasonable accuracy of the model at an increasing range of St_h, St_θ and ϕ. We also depict vertical iso-lines in figure 11 that correspond to the model output ≈ 0.4 and 1.5. These further mark the approximate bounds where a particular wake topology will dominate for a specific combination of St_h, St_θ and ϕ. Kinematic setting corresponding to the left of iso-line 1 shows a dominant $2P + 2S$ wake mode, based on the observations from phase maps depicted in figure 7. Between iso-lines 1 and 2, the $2P$ mode dominates the wake. The specific bounds associated with the $2P$ wake mode with vortex bifurcation ($2P^D$ pairs) occur within the region bounded by iso-lines 1 and 2. The region to the right of iso-line 2 depicts the dominance of the *rBvK* wake mode while the $2P$ mode is entirely absent. Overall, (3.16) constitutes a novel relationship that best describes the transition of wake topology for an oscillating foil with combined motion, based on most critical kinematic parameters, including pitching (St_θ) and heaving (St_h) Strouhal numbers, and phase offset (ϕ).

3.5. *Evaluation of wake mode transition at Re* = 4000

To identify the topological transition features of wake modes, the validity of the mathematical model (i.e. (3.13) and (3.15)) and the existence of bifurcations in $2P$ mode at increased *Re*, we now present the phase maps in ϕ–St_c and A_c–St_c phase spaces at

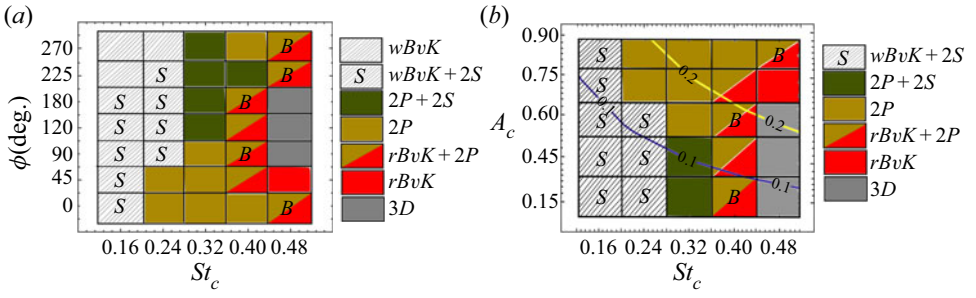

Figure 12. Phase map representation of identified wake modes at increasing St_c, ϕ and A_c for $Re = 4000$.

$Re = 4000$ in figure 12. We observe that at low $St_c < 0.24$, $wBvK$ mode is supplemented by the shedding of two additional single vortical structures, thus representing the configuration as a $wBvK + 2S$ mode. At $St_c > 0.32$, existence of bifurcation is revealed, although an additional $rBvK$ vortex street also co-exists with $2P$ mode. Thus the resulting wake mode is categorized as $rBvK + 2P$. The $rBvK + 2P$ mode also appears at an increased St_c of 0.48.

On the A_c–St_c phase space shown in figure 12(*b*), we observe a transition from $wBvK + 2S$ to $2P$ mode that coincides roughly with the line of $St_A = 0.1$. Beyond $St_A = 0.2$, the $2P$ mode transitions to either $rBvK$ or $rBvk + 2P$ mode. We also observe that the bifurcations in $rBvK + 2P$ mode do not coincide or fall within any threshold St_A, which is in contrast to the observations at $Re = 1000$ (see figure 7*b*). These bifurcations are noticeable at increased St_c and in the entire range of A_c assumed in our study. On account of the above noted observations in A_c–St_c phase space, it can be deduced further that the mathematical relationship outlined in (3.13) and (3.15) may not provide an accurate prediction of wake transition at a higher Re of 4000. The limitation of our model, as stated above, could also indicate that there are other possible effects on vorticity production at higher Re, besides strengthening of the trailing edge vortex structures with increasing St_A (as suggested by (3.13)). This would then make the approximation of leading and trailing edge vortex strengths inaccurate in (3.4) and (3.9). These relationships used in Schnipper *et al.* (2009) have been validated only at Re close to 1000, which were further confirmed in our study as well. Thus an extensive analysis is still needed to address this limitation in the application of our mathematical model over a range of Re. It is also important to note that studies and models concerning phase space representation of wake modes and their transition (Godoy-Diana *et al.* 2008, 2009; Deng *et al.* 2015; Sun, Deng & Shao 2018; Zheng *et al.* 2019) were also limited to $1000 < Re < 1500$. The mechanism of transitioning wake topology and bifurcations of vortex pairs in $2P$ mode at $Re = 4000$ could further reveal differences in wake evolution that could hint at weakness of the mathematical model in predicting the changes in spatial topologies of $2P$ mode.

In order to highlight the transitions in wake topology and presence of bifurcations in $rBvK + 2P$ mode at $Re = 4000$, figure 13 depicts qualitatively the modes in the range $0° \leq \phi \leq 180°$ at $St_c = 0.4$. The wake is dominated by a $2P$ mode at $\phi = 0°$, which is similar to the observations at $Re = 1000$ (see figure 8*a*). The paired trailing and leading edge vortex structures retain coherence only for a short while, after which the similar-sign neighbouring structures merge to form a single coherent structure shown in figure 13(*a*). At $\phi = 45°$, an $rBvK$ mode is observed in figure 13(*b*), which is characterized by shedding of strong trailing edge structures that advect close to the wake centreline. In addition, we

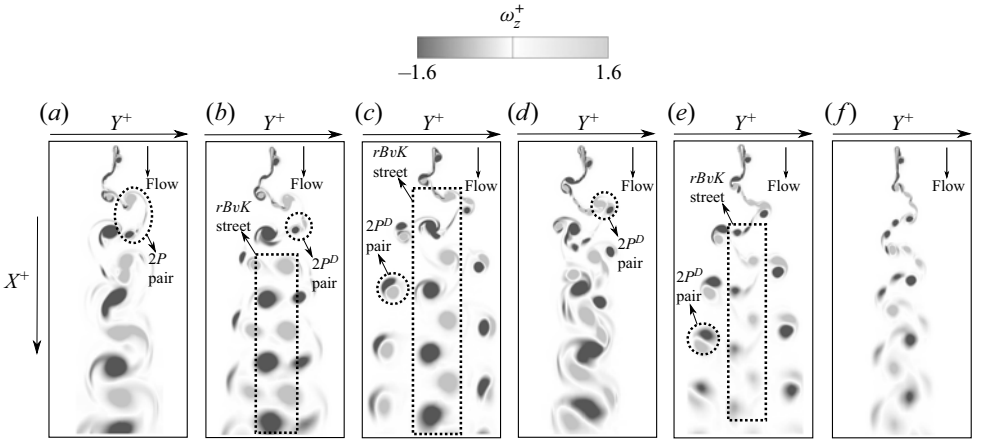

Figure 13. Wake modes at increasing ϕ and $Re = 4000$. Panels (a–f) represents ϕ corresponding to 0°, 45°, 90°, 120°, 180° and 225°, respectively, while $St_c = 0.4$.

see dipole-like paired counter-rotating structures ($2P^D$ pairs) that possess weaker strength compared to the trailing edge structures characterizing the *rBvK* mode. Further, one of the vortical structures constituting this $2P^D$ pair also undergoes stronger stretching in comparison to its counterpart. This $2P^D$ pair, however, does not diverge away from the wake centreline as seen in figure 13(b). On account of the combined presence of features characterizing *rBvK* and 2*P* modes, the resulting wake configuration was termed *rBvK* + 2*P* in figure 12(b).

Vortex streets that depict clear bifurcation in addition to the advecting *rBvK* structures are observed along the wake centreline with increasing ϕ to 90° (figure 13c). The counter-rotating vortical structures constituting these streets also resemble the dipole-like configuration observed previously for $2P^D$ pairs at $Re = 1000$. We see further that the vortical structures associated with *rBvK* mode have more circulation strength and larger size compared to the dipole-like paired structures. This characteristic, however, undergoes a reverse transition at $\phi = 120°$, where the dipole-like paired vortices possess qualitatively a greater strength and size compared to *rBvK* structures. We see further that during this transition at $\phi = 120°$, the similar-sign vortices associated with bifurcated vortex streets and the *rBvK* street, respectively, merge and form single coherent structures approximately around the middle (streamwise) of the wake. A bifurcation of dipole-like pairs is again visible while increasing ϕ to 180° (figure 13e), although the weaker *rBvK* street along the wake centreline is now more vivid compared to $\phi = 120°$. The transition and appearance of bifurcated vortex streets in the wake associated with higher *Re* therefore show different wake features compared to the wakes identified at lower *Re* in figure 8. Here, we first observe formation of dipole-like $2P^D$ pairs in conjunction with *rBvK* structures at $\phi = 45°$. Typically, the individual vortices forming the $2P^D$ pair possessed lower strength and size compared to the vortical structures that constitute the *rBvK* street. However, the $2P^D$ pairs undergo a consistent increase in their strength and size compared to the *rBvK* structures with increasing ϕ from 45° to 180°. The diverging vortical streets comprising the $2P^D$ pairs are observed at $\phi = 90°$, which then appeared to resist their movement away from the wake centreline as ϕ increases to 120°. A re-emergence of a bifurcated vortex street was then observed at $\phi = 180°$. We believe that this dynamic change in the

behaviour of bifurcated dipolar streets could be associated directly with the consistent increase, and decrease, in the strength and size of structures, which constitute bifurcated vortex streets and $rBvK$ wake, respectively. A more closer attention to the formation mechanism will reveal further details of the transitions of modes observed here. Finally, at $\phi = 225^\circ$ (figure 13f), the wake again represents a $2P + 2S$ mode, which was even observed and discussed in figure 8(f) at $Re = 1000$. Thus the unique observations and characterization of bifurcations in $2P$ mode still hold for a higher Reynolds number, although there are additional complexities observed in terms of a combined $rBvK + 2P$ mode.

3.6. *Formation mechanism of $rBvK + 2P$ mode and symmetric bifurcations*

The wake modes observed for increasing St_c and ϕ at $Re = 4000$ were characterized by an $rBvK + 2P$ configuration, where the $2P$ mode observed at $Re = 1000$ is supplemented with an $rBvK$ vortex street. Figure 14 shows the formation and temporal evolution of wake structures constituting the $rBvK + 2P$ mode, along with observed bifurcation of $2P^D$ pairs, at $Re = 4000$. As the oscillation cycle begins (i.e. at $t = 0$) in figure 14(a), we observe a very similar shedding pattern near the trailing edge compared to $Re = 1000$ (see figure 9). The counter-rotating leading and trailing edge structures form an approximate dipole-like paired configuration in each half shedding cycle, which then detaches from the trailing edge. Two dipole-like structures, marked as $D1'$ and $D2'$, are shown in figure 14(a). The dipole-like $2P^D$ pair then moves away from the wake centreline on account of the mutual induced velocity of the pair. However, as the dipole-like structures advect downstream, we observe that an elongated leg of the trailing edge vortex shed in the previous half shedding cycle splits into two structures. This splitting phenomenon was not observed for the $2P$ mode formation at $Re = 1000$. At $t = T/4$ in figure 14(b), we observe vortical structures $\mathrm{TEV1}^s_{ac}$ and S_{ac}, which form due to the splitting of the vortex leg shown in figure 14(a). It is further seen that $\mathrm{TEV1}^s_{ac}$ constitutes a dipole-like configuration of diverging vortex street, while S_{ac} eventually becomes a part of the $rBvK$ wake. A similar splitting process again starts at the end of the first half oscillation cycle, shown in figure 14(c). However, the sense of rotation for the trailing edge vortex leg is opposite to that of the first half shedding cycle. The resulting split structures $\mathrm{TEV2}^s_c$ and S_c are shown in figure 14(d). These structures contribute further to the formation of $rBvK + 2P$ mode. This characterization constitutes a new wake mode that has not been observed previously for bluff bodies or oscillating foils. It also accounts for a very different wake dynamics observed for oscillating foils with combined heaving and pitching motion, compared to those with either pure heaving or pure pitching kinematics.

The shear splitting phenomenon that explained reasonably the formation process of $rBvK + 2P$ and coinciding bifurcation could also provide insights into the disappearance and re-emergence of the birfurcated dipole streets observed and highlighted in the previous subsection. As ϕ increases from 45° to 180°, we observed (figures 13b–e) that a clear bifurcation of dipole-like pairs appears in conjunction with the $rBvK$ structures for $\phi = 90^\circ$. However, at $\phi = 120^\circ$, the bifurcation was not imminent. Further increase in ϕ to 180° depicted a reappearance of bifurcation for the dipole-like pairs. As indicated earlier, there is a consistent decrease in strength of trailing edge vortical structures relative to the structures forming at the leading edge. This change has a direct consequence on the shear splitting phenomenon where a delay in splitting of the trailing edge vortex leg occurs as ϕ increases from 45° to 180°. We provide qualitative evidence in figure 15, which depicts the shear splitting process for wake observed at $Re = 4000$, and $\phi = 45^\circ, 90^\circ, 120^\circ$

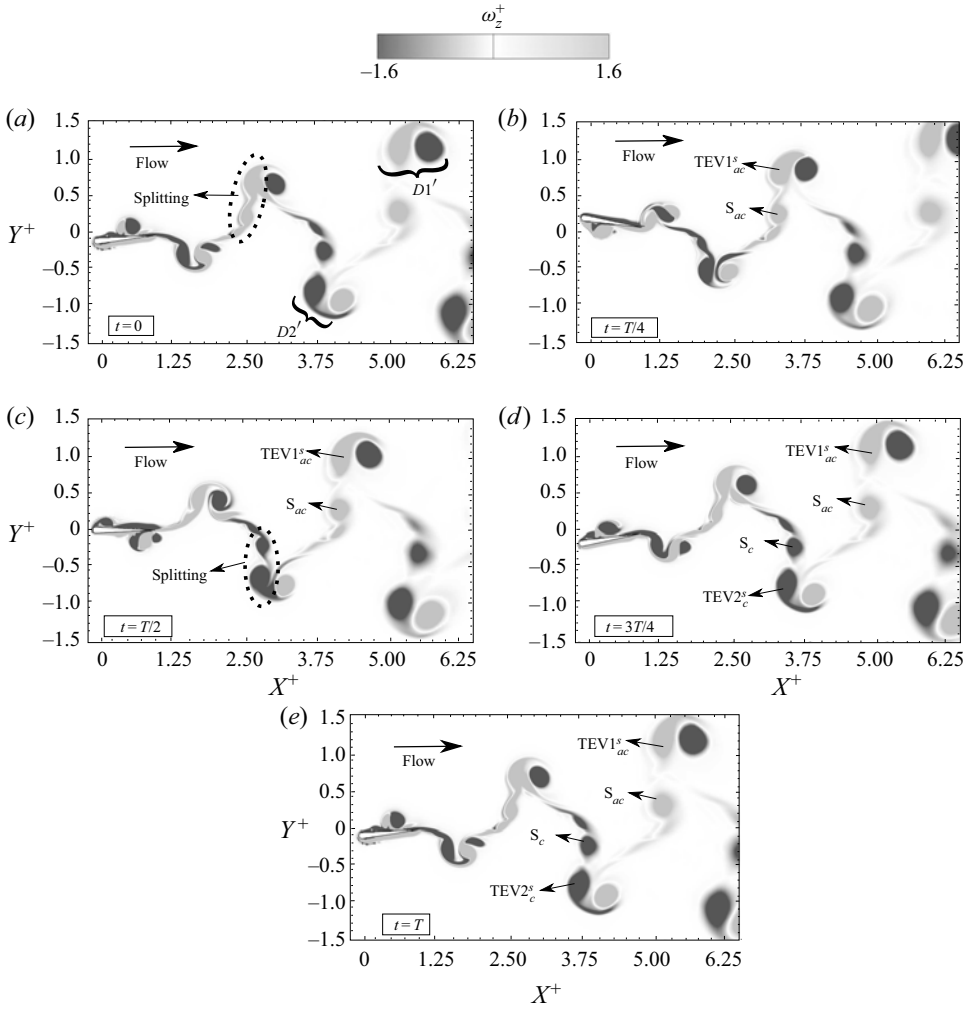

Figure 14. Temporal snapshots representing contours of $\omega_z^+ = \omega_z c/U_\infty$, and depicting formation of $rBvK + 2P$ mode with bifurcation at $Re = 4000$.

and 180°, respectively. At $\phi = 45°$ (figure 15*a*), we see that as the trailing edge vortex separates from the trailing edge, the dipole-like pair (D) is well detached, devoid of any mutual interaction with the trailing edge vortex leg. As ϕ increases to 90° (see figure 15*b*), the dipole-like pair (D) now appears close to the detached trailing edge vortex while also undergoing mutual interaction with its leg. Thus a delay is observed in the splitting process with the weakening of the trailing edge vortex. Further increasing ϕ to 120°, the splitting is further delayed compared to $\phi = 90°$. The weaker trailing edge vortex strength compared to vortical structures constituting D is also observed in figure 15(*c*). At $\phi = 180°$ (see figure 15*d*), only the dipole-like pair D appears well developed, with the splitting process undergoing an even greater delay compared to the cases at lower ϕ. The bifurcation of dipole streets that occurs at $\phi < 120°$ could be attributed to the rapid splitting process that happens on account of the longer trailing edge vortex development. However, bifurcation

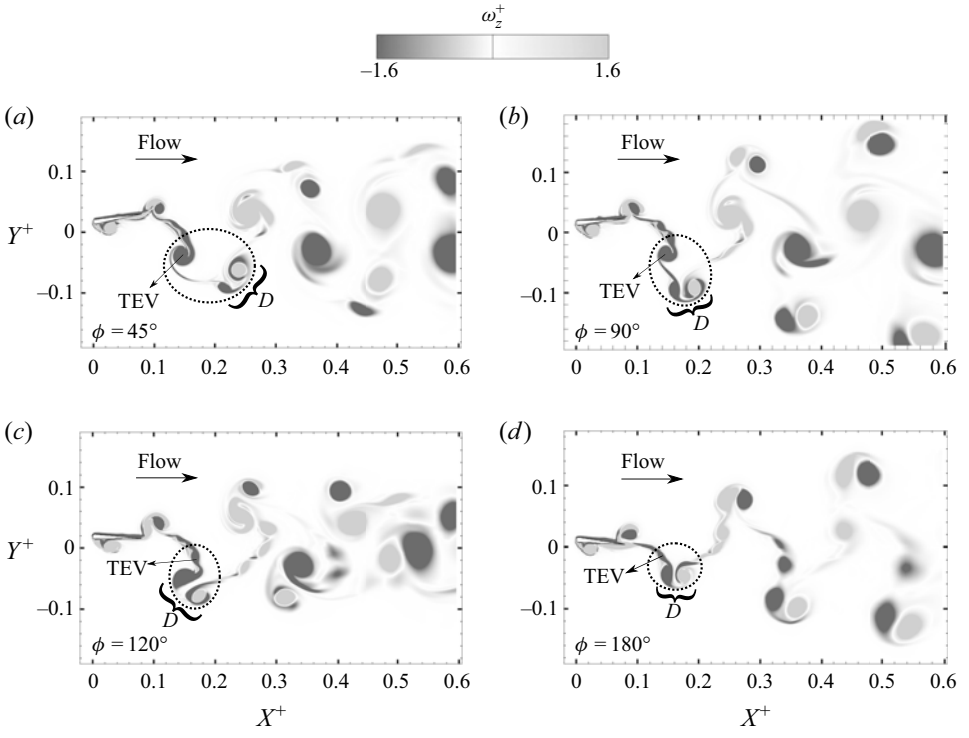

Figure 15. Changes in the dynamic shear splitting process with increasing ϕ.

observed at $\phi > 120°$ largely could be a consequence of higher induced velocity of the dipole-like configuration, which further triggers the shear splitting ahead in the wake.

The lack of bifurcated dipole-like streets at $\phi = 120°$ also needs closer attention. Figure 16 depicts the temporal evolution of the trailing edge vortex and dipole-like pair D. Even after the shear splitting (at approximately $t = 0.45T$ in figure 16) occurs, the short separation distance between the clockwise vortex, constituting the dipole pair (D), and the trailing edge vortex promotes a merger rather than movement of D away from the wake centreline. Thus we also see in figure 16(c) that the split trailing edge vortices eventually merge with the similar-sign vortical structures of neighbouring dipoles that further undergo a combined interaction near the wake centreline. Besides the determination of critical ϕ (i.e. $\phi = 120°$) where the bifurcation disappears and dipole-induced velocity begins to dominate the wake dynamics, a more detailed investigation is underway in a separate study, which will model quantitatively the above transition process.

The splitting observed at $Re = 4000$ provides additional explanations for the potential limitation of the proposed mathematical model in (3.13) and (3.15) for higher Reynolds numbers. The observations of Schnipper *et al.* (2009) indicated no splitting in their wake structures near the foil trailing edge at $Re \approx 1200$. The approximation of downward transport of vorticity, as employed in our study similar to that of Schnipper *et al.* (2009), was based on estimating the vorticity production from Tietjens *et al.* (1957), which does not account for any effect of splitting mechanism in the wake of bluff bodies. As also detailed in the study by Ramesh *et al.* (2012), with regard to unsteady effects on leading edge vortex shedding with increasing Re, the vorticity distribution and thereby the circulation is inherently dependent on the wake-induced downwash velocity in parallel and normal

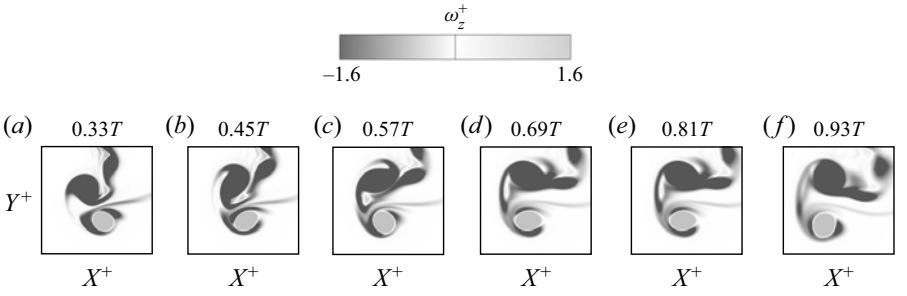

Figure 16. Temporal evolution of wake splitting and merging at $\phi = 120°$.

directions to the foil chord. This wake-induced velocity at $Re = 4000$ will not be similar to the approximation (Ramesh *et al.* 2012) that holds at $Re = 1000$ due to the onset of unsteady splitting mechanisms in the near wake. This attributes directly to the inaccuracy in estimating circulation of the leading edge, or boundary layer, vortices (i.e. (3.4)). A similar observation holds for the study of Schnipper *et al.* (2009). This provides a reasonable explanation for why our newly proposed mathematical model does not work well in predicting the transition in wake topological characteristics at higher Reynolds numbers, e.g. $Re = 4000$.

The higher complexity of wake dynamics observed at $Re = 4000$ also hints at a reason for the lack of correspondence between the $rBvK + 2P$ mode (and the observed bifurcation) and the pitch- or heave-dominated kinematics. The qualitative and quantitative observations of $2P$ mode at $Re = 1000$ suggested that the equalization of strength and size of leading and trailing edge vortices are the only prominent contributing aspects for the observed bifurcated streets at higher Reynolds numbers, which coincided only with heave-dominated kinematics at low Re. However, the qualitative transition and formation mechanisms at $Re = 4000$ revealed a shear splitting process that was not seen at $Re = 1000$. This phenomenon also depicted varying temporal characteristics as the kinematics switch from pitch- to heave-dominated kinematics based on ϕ. We believe that since the dominance of this splitting process (responsible for formation of bifurcated vortex streets) at $Re = 4000$ is not limited within certain regimes of prescribed kinematics for the foil, such bifurcations in $rBvK + 2P$ wake mode can appear in different kinematic settings that induce similar effects, such as $St_c = 0.48$ at $Re = 4000$ (see figure 12*b*).

3.7. *Mean flow development in bifurcated dual vortex street wakes*

In order to characterize the bifurcated dual vortex streets in $2P$ and $rBvK + 2P$ wake modes, we now evaluate the qualitative and quantitative time-averaged streamwise velocity ($\overline{U_x^+}$) distribution in the wake. Figure 17 shows the contours of $\overline{U_x^+}$ for increasing ϕ at $St_c = 0.4$ and $Re = 1000$. Although we depict the contours corresponding to only cases $\phi = 0°$, 90°, 180° and 225°, the quantitative profiles in figure 18 are shown for all ϕ values ranging from pitch- to heave-dominated motion kinematics. These profiles are further obtained at three streamwise locations corresponding to $X^+ = 1.5$, 3.5 and 5.5, respectively, as shown in figure 17(*a*). Due to similarities in the mean characteristics for some cases (e.g. $\phi = 90°$ and 120°), contours for only some cases are shown, for brevity.

The mean velocity excess at the wake centreline ($Y^+ = 0$) is maximum in the case of $\phi = 0°$ and 45°, at all three X^+ locations (see figure 18). However, a mean velocity deficit

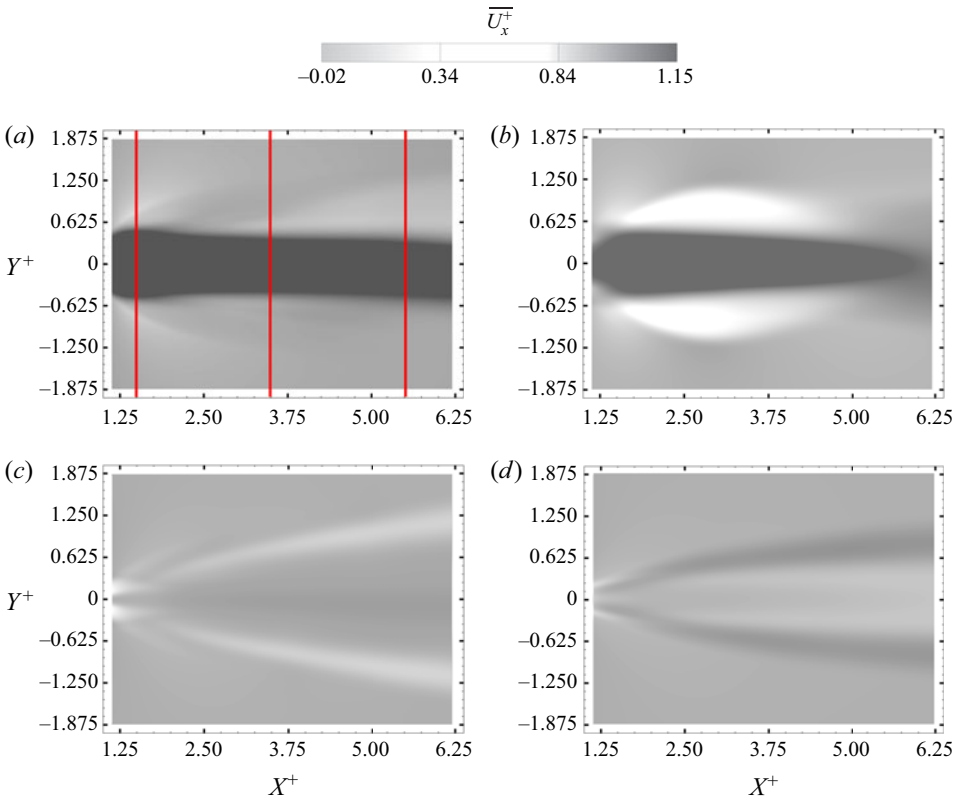

Figure 17. Contours of $\overline{U_x^+}$ at (*a*) $\phi = 0°$, (*b*) $\phi = 90°$, (*c*) $\phi = 180°$, and (*d*) $\phi = 225°$. Solid red lines depict the streamwise locations where cross-stream profiles of $\overline{U_x^+}$ are extracted and shown in figure 18.

region is also observed for $\phi = 45°$, which strengthens further with increasing X^+. These deficit regions are also observed alongside the mean thrust jet developing in the wake.

Earlier, we discussed the upstream tilted vortex pairs depicted for $\phi = 45°$ in figure 8(*b*), which did not show a significant merger between the neighbouring vortex structures with a similar sense of rotation. These tilted pairs promote creation of a resultant induced velocity that acts against the freestream. Therefore, it results in the dual velocity deficit regions observed for the case $\phi = 45°$. Such tilted pairs, however, were not seen at $\phi = 0°$ in figure 8(*a*). Increasing ϕ to 90° showed a transition of counter-rotating paired vortex structures to a dipole-like formation in figure 8(*c*). This coincides clearly with a reduction in the peak magnitude of the mean thrust jet, compared to the lower ϕ cases observed in figure 18. This jet is also shortened in terms of its streamwise extent, as shown in figure 17(*b*). This is also confirmed by the sharp drop in the peak velocity at $Y^+ = 0$ in figure 18(*c*) for the wakes of $\phi \geq 90°$. Despite this decrease along the wake centreline, the neighbouring minima decrease further as ϕ increases to 120°. This is observed specifically for the streamwise locations corresponding to $X^+ = 1.5$ and 3.5, respectively. For $X^+ = 5.5$, however, the velocity deficit regions flatten with increasing ϕ to 120°. These observations also coincide with the vortex interaction and merger observed for $\phi = 90°$ and 120° in figures 8(*c*) and 8(*d*), respectively. Since these merged structures advect closely along the wake centreline in figures 8(*c*,*d*), resultant induced velocity must be insignificant. Thus it leads to flat velocity profiles along Y^+.

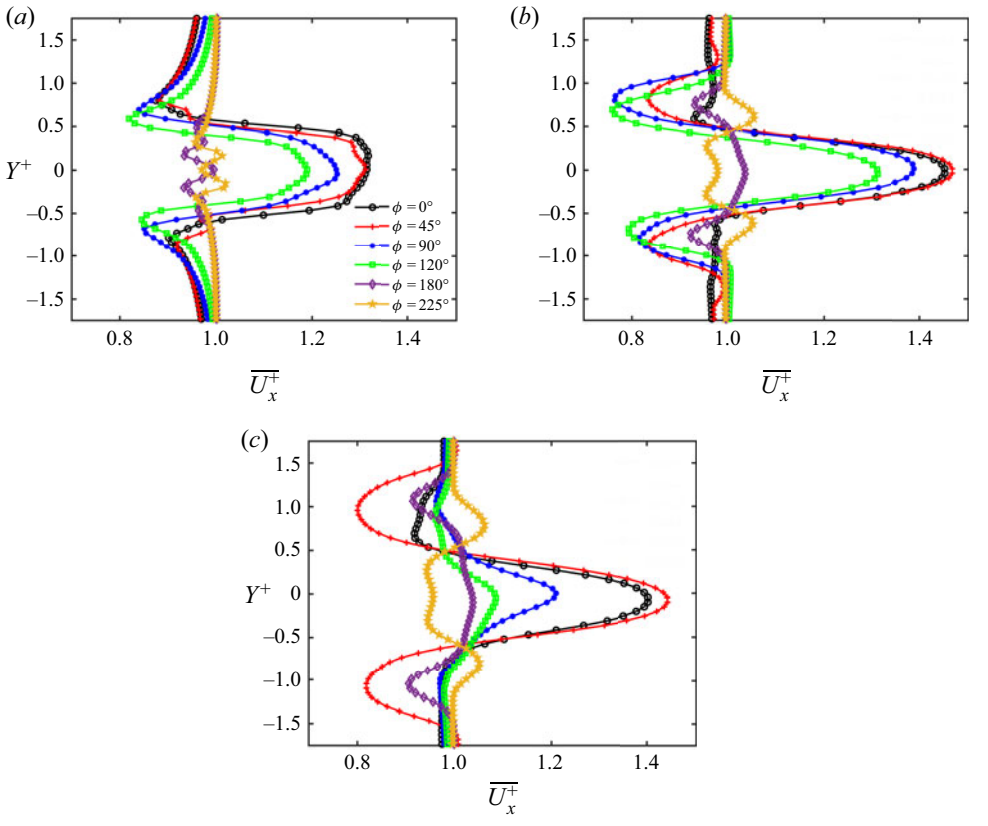

Figure 18. Profiles of $\overline{U_x^+}$ along the cross-stream (Y^+) direction at streamwise locations corresponding to (*a*) $X^+ = 1.5$, (*b*) $X^+ = 3.5$, and (*c*) $X^+ = 5.5$.

At $\phi = 180°$, the cross-stream profiles for $\overline{U_x^+}$ show a different characteristic time-averaged wake. Near the foil, a pair of velocity minima is observed in figure 18(*a*), with a relatively minor drop compared to U_∞, which is close to the wake centreline. Assessment at increasing streamwise distance from the foil reveals further that the minima locations disperse away from the wake centreline. This feature coincides with the diverging dual vortex streets seen in figure 8(*e*). This is confirmed qualitatively in figure 17(*c*), which identified the presence of diverging velocity deficit streams along the streamwise direction. As ϕ is increased further to 225°, we observe two velocity maxima or peaks that neighbour the wake centreline. This feature, observed from the quantitative profiles depicted in figure 18, is in definite contrast to the characteristics observed at $\phi = 180°$. However, the twin peaks move away from the wake centreline in a fashion similar to the minima locations observed at $\phi = 180°$. This feature is also noticeable in figure 17(*d*), where we observe two streams of relatively high mean velocity in the wake. From the above observations, it is seen that the formation of diverging vortex streets at $\phi = 180°$ reflects a critical threshold characteristic, since the mean wake features deviate and follow different spatio-temporal development as ϕ is switched away from 180°. These dual dipole-like vortex streets are also suggestive of a relatively low spatial disturbance near the wake centreline region, compared to mean wake features associated with ϕ values higher or lower than 180°.

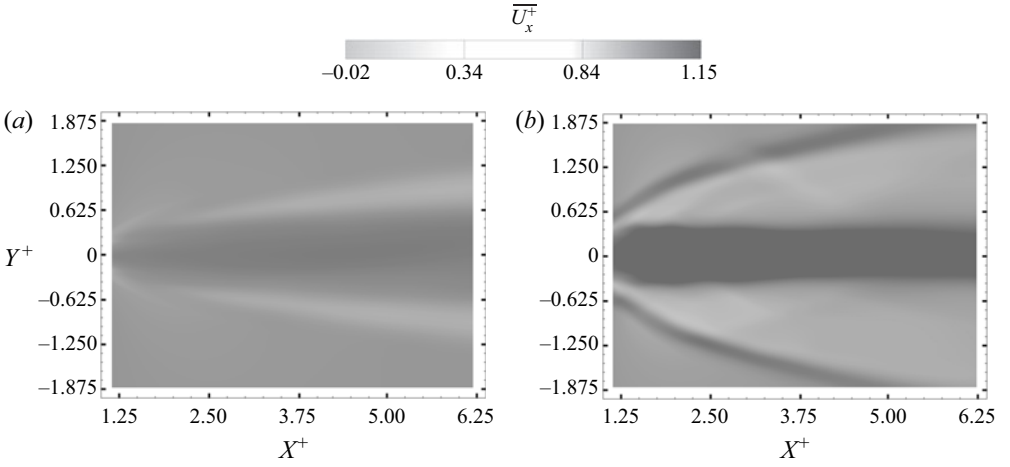

Figure 19. Contours of $\overline{U_x^+}$ at (*a*) $\phi = 225°, f^* = 0.48$, $Re = 1000$, and (*b*) $\phi = 90°, f^* = 0.4$, $Re = 4000$.

Figure 19(*a*) depicts further the contours of $\overline{U_x^+}$ for $\phi = 225°$ at $f^* = 0.48$ and $Re = 1000$. This kinematic and flow configuration corresponded to the $2P$ mode in which bifurcations were evident, as identified in figure 7(*a*). It is observable that the mean spatial development coinciding with the bifurcated dual vortex street remains largely unaffected with increased St_c. The diverging velocity deficit streaks appear comparatively similar to the $\overline{U_x^+}$ development observed in figure 17(*c*), which corresponds to the case $\phi = 180°$ and $f^* = 0.4$. A spatial uniformity in the cross-stream distribution of $\overline{U_x^+}$ is also retained at this higher St_c setting. Figure 19(*b*), however, depicts the $\overline{U_x^+}$ distribution at a higher Re of 4000, while ϕ and St_c correspond to 90° and 0.4, respectively. This setting also coincides with the $rBvK + 2P$ mode identified in figure 12(*b*), which underwent bifurcation and whose formation was also discussed in a previous subsection. A relatively strong thrust jet is seen along the wake centreline on account of the $rBvK$ vortex street observed in figure 13(*c*). We also see two bifurcated streaks that possess a relatively higher velocity compared to the surrounding flow. Such bifurcation in mean flow is again suggestive of an implication posed by dual vortex streets in $rBvK + 2P$ mode. However, these weak jet streaks still appear in contrast to the velocity deficit streaks observed at lower Re, and which corresponded to only a $2P$ mode (see figures 17*c* and 19*a*).

4. Conclusions

The wake characteristics of an oscillating foil in combined heaving and pitching motion were evaluated numerically with respect to increasing phase offset ($0° \leq \phi \leq 270°$), chord-based Strouhal number ($0.16 \leq St_c \leq 0.48$) and Reynolds number. Increasing Strouhal number and phase offset within the considered range constitute a transition of kinematics from pitch- to heave-dominated oscillatory motion, which brings about a unique transition in wake topology. This transition is characterized by bifurcated dual vortex streets in $2P$ mode. These streets exhibited counter-rotating vortical structures with mutual pairing within a half shedding cycle that resembled the mechanism of a $2P$ wake (Williamson & Roshko 1988; Schnipper *et al.* 2009). However, qualitative and quantitative characteristics of the wake evolution, such as circulation strength and separation distance, showed resemblance of vortex dipoles or couples. Both leading and trailing edge vortices

were observed further to contribute to the formation of dipole-like configurations ($2P^D$ pairs) that dominated the $2P$ mode. Although this characteristic of $2P^D$ pairs resembled some similarities with the Mode-1 configuration described previously by Cleaver *et al.* (2011), the $2P$ wake observed here exhibited no merger between similar-sign leading and trailing edge vortices. Further, the findings noted here were also in definite contrast to the observations made for typical vortex dipoles that are formed only on account of trailing edge structures (Cleaver *et al.* 2012; Calderon *et al.* 2014; He & Gursul 2016; Verma & Hemmati 2021*b*).

This wake mechanism was also modelled mathematically, where the relative circulation strengths of counter-rotating vortical structures was found to depend on the foil kinematics, including pitching amplitude (St_A), heaving amplitude (St_h), trailing edge amplitude (St_θ), and the phase offset (ϕ) between the heaving and pitching motion. The model suggested that at constant St_h, an increase in ϕ up to 180° would lead to a decrease in St_A, which thereby reduces the relative circulation strength ratio of counter-rotating structures from the trailing and leading edges of the foil. The quantitative estimation of the relative circulation strength from the numerical data confirmed the model findings for ϕ greater than 45°, corresponding to heave-dominated kinematics at constant $St_h = 0.2$ and $St_c = 0.4$, where the bifurcations in $2P$ mode were observed. The phase map characterized by increasing A_c–St_c also validated the predictions of the proposed mathematical model. With increasing St_A, qualitatively the wake modes depicted transition from $2P$ wake topologies to *rBvK* mode. This agreed with previously reported wake dynamics, where an increase in St_A corresponded to an increased relative strength in the trailing edge vortex, and hence led to a transition of wake towards an *rBvK* topology. The proposed model was further found accurate in predicting the trends for circulation strength ratio of trailing and leading edge structures, at increasing St_h, St_θ and ϕ, while also providing the approximate bounds (in terms of model output) where the major wake mode configurations like $2P$, $2P + 2S$ and *rBvK* are dominant.

The wake mode transition identified at a higher Re of 4000 revealed a similar novel wake configuration that is characterized by secondary formation of an *rBvK* vortex street, and accompanied with the bifurcated dual vortex streets of $2P$ mode. Besides the shear splitting phenomenon that is responsible for the growth of the *rBvK* street in conjunction with the $2P$ mode, the transition in spatial characteristics of shed vortical structures also showed a distinct signature in the wake. Here, the coherent structures that dominated the *rBvK* street lost their circulation strength consistently with increasing ϕ to 180°, while the $2P$ mode structures became relatively stronger. This mechanism coincided with a loss and subsequent reappearance of dual bifurcated vortex streets at $\phi = 120°$ and 180°, respectively. Further evaluation of this unique transition mechanism at $Re = 4000$ revealed that with increasing ϕ from 45° to 180°, the shear splitting process undergoes a consistent delay. This coincides with increasing strength of dipole-like paired structures. The contribution of the splitting process that was dominant at $\phi < 120°$ reduced with increasing ϕ from 120° to 180°. The induced velocity of the dipole pair was the dominating factor that prompted the formation of bifurcated dipole streets. The mathematical relationship between relative circulation strength of trailing and leading edge vortex structures, and St_A, did not hold well at higher Reynolds numbers (e.g. $Re = 4000$) in the qualitative sense. This was possibly on account of changes imposed on approximation for vorticity production at higher Reynolds numbers with increasing St_c. Further, the approximation of circulation of leading edge vortex structures appears inadequate on account of its failure to include effects of splitting process observed in the near wake at $Re = 4000$. The qualitative result of wake transition thus suggested that a

distinct transition among $2P$ and $rBvK$ type modes does not coincide within a specific St_A threshold, as observed at $Re = 1000$.

Mean spatio-temporal wake characteristics revealed low disturbance in the cross-stream mean velocity profile associated with the birfurcated dual vortex streets of $2P$ mode. This feature was found consistent with increased streamwise distance along the wake. However, the mean velocity distribution corresponding to ϕ values lower or higher than 180° appeared in contrast to those associated with the $2P$ mode that experiences bifurcation. For the $rBvK + 2P$ mode observed at a higher Re, a mean thrust jet also accompanied the weak bifurcated streaks that were characterized by minor increase in velocity compared to the surrounding flow. The thrust jet was formed on account of the $rBvK$ vortex street observed in addition to the $2P$ mode at higher Re. Such mean flow characteristics corresponding to bifurcated dual vortex streets are therefore suggestive of novel flow control mechanisms. The dual vortex streets of $2P$ mode can be useful specifically in scenarios where the incoming flow is required to be manipulated such that the wake behind an oscillating body is free from substantial jet development or a recirculating flow. In situations where segregated mean thrust profile is warranted for design improvements, the bifurcations instilled in $rBvK + 2P$ mode could be useful in flow manipulation.

Funding. This research has received support from the Canada First Research Excellence Grant. The computational analysis was completed using Compute Canada clusters.

Declaration of interests. The authors report no conflict of interest.

Author ORCIDs.
Suyash Verma https://orcid.org/0000-0001-6395-2533;
Arman Hemmati https://orcid.org/0000-0002-8897-4525.

References

Andersen, A., Bohr, T., Schnipper, T. & Walther, J.H. 2017 Wake structure and thrust generation of a flapping foil in two-dimensional flow. *J. Fluid Mech.* **812**, R4.

Anderson, J.M., Stretlien, K., Barrett, D.S. & Triantafyllou, M.S. 1998 Oscillating foils of high propulsive efficiency. *J. Fluid Mech.* **360**, 41–72.

Bode-Oke, A.T. & Dong, H. 2020 The reverse flight of a monarch butterfly (*Danaus plexippus*) is characterized by a weight-supporting upstroke and postural changes. *J. R. Soc. Interface* **17** (167), 20200268.

Bose, C., Gupta, S. & Sarkar, S. 2021 Dynamic interlinking between near- and far-field wakes behind a pitching–heaving airfoil. *J. Fluid Mech.* **911**, A31.

Calderon, D.E., Cleaver, D.J., Gursul, I. & Wang, Z. 2014 On the absence of asymmetric wakes for periodically plunging finite wings. *Phys. Fluids* **26** (7), 071907.

Carr, L.W. 2012 Progress in analysis and prediction of dynamic stall. *J. Aircraft* **25** (1), 6–17.

Cimarelli, A., Franciolini, M. & Crivellini, A. 2021 On the kinematics and dynamics parameters governing the flow in oscillating foils. *J. Fluids Struct.* **101**, 103220.

Cleaver, D.J., Wang, Z. & Gursul, I. 2012 Bifurcating flows of plunging aerofoils at high Strouhal numbers. *J. Fluid Mech.* **708**, 349–376.

Cleaver, D.J., Wang, Z., Gursul, I. & Visbal, M.R. 2011 Lift enhancement by means of small-amplitude airfoil oscillations at low Reynolds numbers. *AIAA J.* **49** (9), 2018–2033.

Colgate, J.E. & Lynch, K.M. 2004 Mechanics and control of swimming: a review. *IEEE J. Ocean. Engng* **29** (3), 660–673.

Das, A., Shukla, R.K. & Govardhan, R.N. 2016 Existence of a sharp transition in the peak propulsive efficiency of a low-*Re* pitching foil. *J. Fluid Mech.* **800**, 307–326.

Deng, J., Sun, L. & Shao, X. 2015 Dynamical features of the wake behind a pitching foil. *Phys. Rev.* E **92**, 063013.

Fish, F.E. & Lauder, G.V. 2005 Passive and active flow control by swimming fish and mammals. *Annu. Rev. Fluid Mech.* **38**, 193–224.

FLORYAN, D., VAN BUREN, T., ROWLEY, C.W. & SMITS, A.J. 2017 Scaling the propulsive performance of heaving and pitching foils. *J. Fluid Mech.* **822**, 386–397.

GODOY-DIANA, R., AIDER, J.-L. & WESFREID, J.E. 2008 Transitions in the wake of a flapping foil. *Phys. Rev.* E **77**, 016308.

GODOY-DIANA, R., MARAIS, C., AIDER, J.L. & WESFREID, J.E. 2009 A model for the symmetry breaking of the reverse Bénard–von Kármán vortex street produced by a flapping foil. *J. Fluid Mech.* **622**, 23–32.

GUNGOR, A. & HEMMATI, A. 2021 The scaling and performance of side-by-side pitching hydrofoils. *J. Fluids Struct.* **104**, 103320.

HE, X. & GURSUL, I. 2016 Point vortex model of deflected wakes of oscillating airfoils. *AIAA J.* **54** (11), 3647–3651.

HEMMATI, A., VAN BUREN, T. & SMITS, A.J. 2019 Effects of trailing edge shape on vortex formation by pitching panels of small aspect ratio. *Phys. Rev. Fluids* **4**, 033101.

HULTMARK, M., LEFTWICH, M. & SMITS, A.J. 2007 Flowfield measurements in the wake of a robotic lamprey. *Exp. Fluids* **43**, 683690.

KOOCHESFAHANI, M.M. 1989 Vortical patterns in the wake of an oscillating airfoil. *AIAA J.* **27** (9), 1200–1205.

LAGOPOULOS, N.S., WEYMOUTH, G.D. & GANAPATHISUBRAMANI, B. 2019 Universal scaling law for drag-to-thrust wake transition in flapping foils. *J. Fluid Mech.* **872**, R1.

LENTINK, D., MUIJRES, F.T., DONKER-DUYVIS, F.J. & VAN LEEUWEN, J.L. 2008 Vortex–wake interactions of a flapping foil that models animal swimming and flight. *J. Expl Biol.* **211** (2), 267–273.

LI, C., DONG, H. & ZHAO, K. 2020 Dual functions of insect wings in an odor-guided aeronautic navigation. *Trans. ASME J. Fluids Engng* **142** (3), 030902.

LIGHTHILL, M.J. 1969 Hydromechanics of aquatic animal propulsion. *Annu. Rev. Fluid Mech.* **1** (1), 413–446.

MERRILL, B.E. & PEET, Y.T. 2017 Effect of impinging wake turbulence on the dynamic stall of a pitching airfoil. *AIAA J.* **55** (12), 4094–4112.

MULLER, U.K., VAN DEN BOOGAART, J.G.M. & VAN LEEUWEN, J.L. 2008 Flow patterns of larval fish: undulatory swimming in the intermediate flow regime. *J. Expl Biol.* **211** (2), 196–205.

PETRA, T. 2019 Description of the overset mesh approach in ESI version of OpenFOAM. In *Proceedings of CFD with OpenSource Software, 2019* (ed. H. Nilsson).

POPE, S.B. 2000 *Turbulent Flows*. Cambridge University Press.

RAMESH, K.K., KE, J., GOPALARATHNAM, A. & EDWARDS, J.R. 2012 Effect of airfoil shape and reynolds number on leading edge vortex shedding in unsteady flows. *AIAA Paper* 2012-3025.

SCHNIPPER, T., ANDERSEN, A. & BOHR, T. 2009 Vortex wakes of a flapping foil. *J. Fluid Mech.* **633**, 411–423.

SENTURK, U. & SMITS, A.J. 2018 Numerical simulations of the flow around a square pitching panel. *J. Fluids Struct.* **76**, 454–468.

SENTURK, U. & SMITS, A.J. 2019 Reynolds number scaling of the propulsive performance of a pitching airfoil. *AIAA J.* **57** (7), 2663–2669.

SMITS, A.J. 2019 Undulatory and oscillatory swimming. *J. Fluid Mech.* **874**, P1.

SUN, L., DENG, J. & SHAO, X. 2018 Three-dimensional instabilities for the flow around a heaving foil. *Phys. Rev.* E **97**, 013110.

TIETJENS, O.G., PRANDTL, L. & ROSENHEAD, L. 1957 Fundamentals of hydro- and aeromechanics, p. 270. Dover.

TRIANTAFYLLOU, G.S., TRIANTAFYLLOU, M.S. & GROSENBAUGH, M.A. 1993 Optimal thrust development in oscillating foils with application to fish propulsion. *J. Fluids Struct.* **7** (2), 205–224.

TRIANTAFYLLOU, M.S., TRIANTAFYLLOU, G.S. & YUE, D.K.P. 2000 Hydrodynamics of fishlike swimming. *Annu. Rev. Fluid Mech.* **32** (1), 33–53.

VAN BUREN, T., FLORYAN, D. & SMITS, A.J. 2019 Scaling and performance of simultaneously heaving and pitching foils. *AIAA J.* **57** (9), 3666–3677.

VAN BUREN, T., FLORYAN, D., WEI, N. & SMITS, A.J. 2018 Flow speed has little impact on propulsive characteristics of oscillating foils. *Phys. Rev. Fluids* **3**, 013103.

VERMA, S., FREEMAN, B.R.S. & HEMMATI, A. 2022*a* Effects of Reynolds number and average angle of attack on the laminar scaling of oscillating foils. *Phys. Fluids* **34** (3), 031905.

VERMA, S. & HEMMATI, A. 2020 Performance of overset mesh in modeling the wake of sharp-edge bodies. *Computations* **8** (3), 66.

VERMA, S. & HEMMATI, A. 2021*a* Asymmetry in wake of oscillating foils with combined pitching and heaving motion. In *Progress in Turbulence IX* (ed. R. Örlü, A. Talamelli, J. Peinke & M. Oberlack), pp. 97–102. Springer International Publishing.

VERMA, S. & HEMMATI, A. 2021*b* Evolution of wake structures behind oscillating hydrofoils with combined heaving and pitching motion. *J. Fluid Mech.* **927**, A23.

VERMA, S. & HEMMATI, A. 2022 Route to transition in propulsive performance of oscillating foil. *Phys. Rev.* E **105** (4), 045102.

VERMA, S., KHALID, M.S.U. & HEMMATI, A. 2022*b* On association of lift generation, wake topology and kinematics of oscillating foils. *Intl J. Micro Air Veh.* **14**, 175682932110739.

VIDELER, J.J. 1993 Fish swimming. In *Fish and Fisheries, series 10*. Springer.

VISBAL, M.R. 2009 High-fidelity simulation of transitional flows past a plunging airfoil. *AIAA J.* **47** (11), 2685–2697.

WEBB, P. 1975 Hydrodynamics and energetics of fish propulsion. *Bull. Fis. Res. Board Canada* **190**, 1–156.

WILLIAMSON, C.H.K. & ROSHKO, A. 1988 Vortex formation in the wake of an oscillating cylinder. *J. Fluids Struct.* **2** (4), 355–381.

WU, X., ZHANG, X., TIAN, X., LI, X. & LU, W. 2020 A review on fluid dynamics of flapping foils. *Ocean Engng* **195**, 106712.

ZHENG, H., XIE, F., JI, T., ZHU, Z. & ZHENG, Y. 2020 Multifidelity kinematic parameter optimization of a flapping airfoil. *Phys. Rev.* E **101** (1), 013107.

ZHENG, H., XIE, F., ZHENG, Y., JI, T. & ZHU, Z. 2019 Propulsion performance of a two-dimensional flapping airfoil with wake map and dynamic mode decomposition analysis. *Phys. Rev.* E **99** (6), 063109.

ZURMAN-NASUTION, A.N., GANAPATHISUBRAMANI, B. & WEYMOUTH, G.D. 2020 Influence of three-dimensionality on propulsive flapping. *J. Fluid Mech.* **886**, A25.